water

MDPI

Article

Enhanced Visible-Light-Assisted Photocatalytic Removal of Tetracycline Using Co/La@g-C_3N_4 Ternary Nanocomposite and Underlying Reaction Mechanisms

Kingsley Igenepo John, Touma B. Issa, Goen Ho, Aleksandar N. Nikoloski and Dan Li *

College of Science, Technology, Engineering & Mathematics, Murdoch University, Murdoch, WA 6150, Australia; kingsleyjohn2020@gmail.com (K.I.J.); t.issa@murdoch.edu.au (T.B.I.); g.ho@murdoch.edu.au (G.H.); a.nikoloski@murdoch.edu.au (A.N.N.)

* Correspondence: l.li@murdoch.edu.au; Tel.: +61-08-9360-2569

Abstract: Graphitic carbon nitride (g-C_3N_4) is a promising material for photocatalytic applications. However, it suffers from poor visible-light absorption and a high recombination rate of photogenerated electron–hole pairs. Here, Co/La@g-C_3N_4 with enhanced photocatalytic activity was prepared by co-doping Co and La into g-C_3N_4 via a facile one-pot synthesis. Co/La@g-C_3N_4 displayed better performance, achieving 94% tetracycline (TC) removal within 40 min, as compared with g-C_3N_4 (BCN, 65%). It also demonstrated promising performance in degrading other pollutants, which was ~2–4-fold greater relative to BCN. The improved photocatalytic activity of Co/La@g-C_3N_4 was associated with improved photogenerated charge separation, reduced charge transfer resistance, a built-in electric field arising from the p-n-p heterojunction, and the synergistic effect of ternary components for the separation and transfer of the photogenerated charge carriers. Superoxide radicals are suggested to be the most notable reactive species responsible for the photocatalytic reaction. Environmental factors, including the pollutant concentration, catalyst dosage, solution pH, inorganic salts, water matrices, and mixture with dyes, were considered in the photocatalytic reactions. Co/La@g-C_3N_4 showed good reusability for five cycles of the photocatalytic degradation of TC. The facile one-pot co-doping of Co and La in g-C_3N_4 formed a p-n-p heterojunction with boosted photocatalytic activity for the highly efficient removal of TC from various water matrices.

Keywords: graphitic carbon nitride; metal; co-doping; photocatalysis; antibiotics; visible light

Citation: John, K.I.; Issa, T.B.; Ho, G.; Nikoloski, A.N.; Li, D. Enhanced Visible-Light-Assisted Photocatalytic Removal of Tetracycline Using Co/La@g-C_3N_4 Ternary Nanocomposite and Underlying Reaction Mechanisms. *Water* **2024**, *16*, 2563. https://doi.org/10.3390/w16182563

Academic Editor: Andrea G. Capodaglio

Received: 13 July 2024
Revised: 11 August 2024
Accepted: 13 August 2024
Published: 10 September 2024

1. Introduction

Since the discovery of Penicillin from *Penicillium* in 1928, there has been a growing number of antibiotics from synthetic and natural sources [1]. Antibiotics are broadly employed to treat or prevent diseases in humans and animals, and a proportion of them are used as growth promoters in animals [2]. Tetracycline (TC) is an antibiotic well known for its broad-spectrum activity against a wide range of Gram-positive and Gram-negative bacteria [3]. Despite the significant importance of TC, its residue in the environment or even in our water supply and irrigation systems has raised public concerns [3]. It may result in the growth of antibiotic-resistant bacteria species [3].

Due to the extensive application and poor adsorption of TC, most of it is excreted through faeces and urine as an unmetallized compound into wastewater. Meanwhile, many antibiotics, including TC, are not effectively removed by most wastewater treatment plants and, in turn, contaminate our ecosystem. Thus, there has been continuous research effort exploring effective techniques for efficient TC removal. Among the various approaches studied so far, photocatalysis has been demonstrated to be a promising and eco-friendly method that works by generating highly reactive radicals or oxidants to mineralize pollutants into harmless substances upon illumination [3].

Graphitic carbon nitride (g-C_3N_4) is one of the most widely studied photocatalyst materials owing to its stability, visible-light absorption, eco-friendliness, and cost-effectiveness [4–6]. Nevertheless, its use has been limited due to the high recombination rate of electron–hole pairs, the small surface area of the material, and the low absorption of visible light (<450 nm) [7]. Therefore, researchers have devoted efforts to modifying g-C_3N_4 using various strategies, including morphology tuning, elemental doping, and heterojunction fabrication [8]. Among them, metal doping into g-C_3N_4 has drawn significant research interest due to its ability to improve visible-light absorption, promote charge separation, reduce electron–hole recombination, and increase the active surface area, which resulted in enhanced performances of photocatalytic reaction [9]. Various metal dopants, including Ba, Er, and Eu, have been tested [10–12]. The resulting single-metal-modified g-C_3N_4 exhibited an enhanced visible-light response and reduced recombination of charge carriers relative to pure g-C_3N_4 for improved TC removal.

In recent years, the interest of researchers has moved to the co-doping strategy, which takes advantage of the potential synergistic effect of two dopants and, in turn, largely enables the tailoring of the photocatalytic activity of the base g-C_3N_4 catalyst [13]. So far, several combinations have been reported for dopant pairs consisting of a metal/non-metal or a non-metal/non-metal, e.g., B/Na, Bi/P, Ce/C, B/Eu, S/Bi, B/Se, S/P, and Mo/P [14–21], with some promising outcomes on the improved photocatalytic degradation of TC. However, the non-metal constituents of such dopant combinations could form recombination centres in the lattice of g-C_3N_4, thereby limiting the photocatalytic performance of the modified sample [22]. Some studies have also indicated the leaching of a non-metal dopant and thus the low stability of the modified photocatalyst [23]. On the other side, when adopting metal/metal co-doping, some metal atoms might replace C or N atoms in the g-C_3N_4 structure and, in turn, enhance the electron delocalization of the intralayer and change the band edge [24], whilst some might be incorporated into the interlayers of the g-C_3N_4 structures and then facilitate charge transfer [25]. Furthermore, the possibly formed unique heterojunction between dissimilar semiconductors can optimize absorption properties, enhance carrier separation, reduce electron recombination, accelerate charge transfer, and promote photocatalytic efficiency [26].

We have noted that, as compared to non-metal/non-metal and metal/non-metal co-doping, so far, the efforts contributed to developing and understanding metal/metal co-doping into g-C_3N_4 for the photocatalytic degradation of organics have been limited [25,27–30], with particularly little focus on pharmaceutical removal [31–33]. Among various metal dopants, the combination of rare-earth metals and transition metals has been explored for various photocatalytic applications [25,31,34–37]. A few have reported on the synthesis of visible-light-active photocatalysts targeting the elimination of pharmaceuticals and thus attracted our research interest. On the one side, cobalt (Co), as one of the popular transition-metal candidates for catalysts due to its high positive potential, has been proven to contribute to a lower energy band gap, a reduced recombination rate of electron–hole pairs, and the extended absorption of the solar spectrum [38,39]. On the other side, the rare-earth metal lanthanum (La) has shown a promising effect in interacting with functional groups of organics and enhancing the photocatalytic ability of g-C_3N_4 [40,41]. Co and La metals can augment the performance of g-C_3N_4 since they are able to capture photo-induced electrons and improve light absorption due to their unfilled 4f and empty 5d orbitals [12,42]. The co-doping of La and Co into g-C_3N_4 could boost the photocatalytic activity of the host material by providing a large number of active sites and lowering the activation energy of the photocatalytic system. However, the impact of La and Co dopants on the photocatalytic activity of bulk g-C_3N_4 for the visible-light-initiated photocatalytic removal of antibiotics has not yet been fully optimized, and the underlying mechanisms are not well understood.

Based on the above, in this study, we utilized a facile and cost-effective one-pot synthesis to prepare a Co_3O_4/g-C_3N_4/La_2O_3 ternary heterojunction composite (denoted by Co/La@g-C_3N_4). Visible light was used to initiate the photocatalytic reaction because of its broader range of the electromagnetic spectrum, which makes it more energy-efficient

and cost-effective as compared with the utilization of UV light. It is also safer for the environment and human health when adopted for various photocatalytic applications. The visible-light-initiated photocatalytic activity of Co/La@g-C_3N_4 was evaluated for TC, MO, MB, and RhB removal. Afterwards, the photocatalytic degradation of TC was optimized by varying the pollutant concentration, solution pH, catalyst dosage, water matrices, and co-existing dyes and ions. The reusability of Co/La@g-C_3N_4 was investigated, along with an exploration of its photocatalytic mechanisms.

2. Materials and Methods

2.1. Synthesis and Characterization

Our photocatalyst samples were prepared via a facile one-pot synthesis. Typically, 10 g of urea ($(NH_2)_2CO$, 99.7% Sigma-Aldrich, Melbourne, Australia), 50 mg of lanthanum nitrate hexahydrate ($La(NO_3)_3.6H_2O$, 99.9%, Sigma-Aldrich, Melbourne, Australia), and 10 mg of cobalt hexachloride ($CoCl_2.6H_2O$, ≥97%, Sigma-Aldrich, Melbourne, Australia) were dissolved in 25 mL of ultra-pure water. The resulting suspension was sonicated for 30 min and then magnetically stirred at 80 °C for 1 h [43]. Afterwards, the solution was dried at 85 °C overnight in an oven, and then the obtained solid was calcined at 550 °C for 2 h (10 °C/min) in a furnace. The final product was designated Co/La@g-C_3N_4. For comparison, La@g-C_3N_4 and Co@g-C_3N_4 were prepared under the same reaction conditions as above but in the absence of $CoCl_2.6H_2O$ and $La(NO_3)_3.6H_2O$, respectively. The sample of pristine g-C_3N_4 was synthesized by heating 10 g of $(NH_2)_2CO$ at 550 °C for 2 h under ambient conditions [34].

X-ray diffraction (XRD) characterization at 2θ = 10–80° was performed by using a Rigaku SmartLab X-ray Diffractometer at a 10°/min scanning rate. The surface morphology was examined through a scanning electron microscope (SEM) using Tescan Clara (Brno, Czech Republic) and a transmission electron microscope (TEM) using TEM-TITAN (Boston, MA, USA). Fourier transform infrared resonance (FTIR, Perkin Elmer, Hopkinton, MA, USA) spectra of the synthesized samples were recorded between 4000 cm^{-1} and 400 cm^{-1} using a Perkin Elmer spectrophotometer. Nitrogen adsorption–desorption analysis was conducted at 77 K using Micromeritics Inc. SAPA 2010 (Norcross, Atlanta, GA, USA). The absorption spectra of the samples were measured using a Perkin Elmer Lambda 750 UV/Vis/NIR spectrophotometer, and the band gap was calculated from the Kubelka–Munk equation, $(\alpha h\upsilon)^2$ versus $h\upsilon$.

2.2. Degradation Experiment

To evaluate the visible-light photocatalytic activity of the synthesized photocatalysts, an experiment on tetracycline (TC, 99.9%, Sigma-Aldrich, Melbourne, Australia) degradation was performed in a cylindrical Pyrex container, which was maintained at a constant room temperature under a Xenon lamp (CEL-HX F300, Beijing, China) with a 420 nm cut-off filter. Unless specified otherwise in the reaction conditions for the photocatalytic degradation of TC, the temperature was maintained at 25 °C, the initial TC concentration was 20 mg L^{-1}, the catalyst dosage was 0.4 g L^{-1}, and the initial pH of the TC solution was 5.05. In a typical experiment, 20 mg of the photocatalyst was dispersed into 50 mL of a TC aqueous solution. Before visible-light irradiation, the reaction solution was agitated for 30 min to reach adsorption equilibrium in the dark. Subsequently, the suspension was illuminated with the simulated visible light for 60 min, and 3 mL aliquots were taken at 10 min intervals. The collected solutions were centrifuged at 12,000 rpm for 5 min to separate photocatalyst solids from the solution. The residual TC concentration in the obtained solution was analysed using a Shimadzu UV/Vis spectrophotometer (Kyoto, Japan). Pollutant removal (%) was calculated using Equation (1), and the rate of degradation was obtained from the nonlinear pseudo-first-order kinetic model in Equation (2) [44,45]:

$$\text{TC removal } (\%) = \left(1 - \frac{C}{C_0}\right) \times 100 \quad (1)$$

$$\frac{-dc}{dt} = kC \quad (2)$$

where C_0, C, k, and t denote the initial concentration (mg L^{-1}), the concentration at a given time (mg L^{-1}), the rate constant of degradation (min^{-1}), and the time of the reaction (min), respectively.

To investigate the applicability of our photocatalyst for TC removal, various dyes, including rhodamine B (RhB, ≥99.5%, Sigma-Aldrich, Melbourne, Australia), methyl orange (MO, 85%, Sigma-Aldrich, Melbourne, Australia), and methylene blue (MB, ≥81%, Sigma-Aldrich, Melbourne, Australia), were selected. Different water matrices were also collected, including tap water (TW), deionized water (DW), and rainwater (RW). Their characteristics are shown in Table S1. The TC solution was adjusted by adding either HNO_3 or NaOH to achieve a pH ranging from 2.0 to 11.5.

The stability and recyclability of the synthesized photocatalyst were analysed by reusing it for 5 consecutive cycles. After each run of photocatalytic degradation, the spent photocatalyst was separated from the solution, washed using water/ethanol, and, lastly, dried in an oven. The concentrations of leached metal ions were quantified using an inductively coupled plasma atomic emission spectrometer (ICP-AES) (Agilent 720 ICP-AES with SeaSpray nebulizer, glass-cyclonic Tracey spray chamber, Niagara Plus and inline filter (Glass Expansion); Temecula, CA, USA).

2.3. Photoelectrochemical Measurements

The photoelectrochemical measurements were performed using a Biologic SP-300 electrochemical workstation (Seyssinet-Pariset, France) with a typical three-electrode system. The reference, counter, and working electrodes were silver/silver chloride (Ag/AgCl), Pt wire, and the selected sample. The working electrode was fabricated as follows: 5 mg of the powder sample was mixed with 10 µL of Trixton-100 (Sigma Aldrich, Melbourne, Australia) and 20 µL of DI water to form a slurry. Subsequently, the slurry was coated on a tape-masked fluorine-doped oxide (FTO) glass slide using the doctor blade method to achieve an exposed active area of the sample of about 1 cm^2. The coated FTO slides were dried at 350 °C for 45 min. The transient photocurrent response was recorded in a 0.1 M Na_2SO_4 electrolyte solution in dark and light modes with an interval of 20 s under visible-light illumination (CEL-HX F300 with a 420 nm cut-off filter; Beijing, China). Electrochemical impedance spectroscopy (EIS) Nyquist plots were obtained over the frequency range of 50 mHz to 100 kHz. Analyses to obtain Mott–Schottky plots were executed at an AC voltage of 10 mV, a potential range of −1.0 V to +1.0 V, and frequencies of 100 Hz, 500 Hz, and 1000 Hz.

2.4. Identification of Active Radical Species and Possible Intermediates

To reveal the dominant active species, benzoquinone (BQ, >98%, Sigma-Aldrich), isopropyl alcohol (IPA, ≥99.0%, Sigma-Aldrich), $AgNO_3$ (≥99.9%, Sigma-Aldrich), sodium ethylenediaminetetraacetate (Na_2EDTA, ≥99.0%, Sigma-Aldrich), and L-Tryptophan (L-Trp., ≥98.0%) were introduced as scavengers for superoxide ($\bullet O_2$), hydroxyl (•OH), electrons (e^-), holes (h^+), and singlet oxygen $^1O_2$, respectively.

The possible intermediates generated were analysed using liquid column–mass spectrometry (LCMS) (Shimadzu LCMS-8045) with a C-18 capillary column (Shim-pack XR ODS III (1.6 µm), 2.0 id × 50 mm) (Kyoto, Japan) at 30 °C for the separation of TC intermediates. The mobile phase comprised HPLC-grade 70% water and 30% methanol with a flow rate of 0.4 mL and an injection volume of 0.5 µL. The mass spectra were obtained using the electrospray ionization (ESI) source at 15 kV. The masses of the intermediates were examined in the range of 100 m/z–500 m/z.

3. Results

3.1. Visible-Light Photocatalytic Activity of Photocatalysts

Figure 1a compares TC removal using Co/La@g-C_3N_4 via 30 min of adsorption in the dark followed by 40 min of photocatalytic degradation under visible-light irradiation to that using pristine g-C_3N_4, Co@g-C_3N_4, and La@g-C_3N_4. In the absence of a catalyst, the control photolysis experiment shows a negligible change in TC concentration, suggesting the good stability of TC molecules under our visible-light source. Pristine g-C_3N_4 exhibited a total TC removal of about 65% after photocatalytic degradation. The metal doping of g-C_3N_4 resulted in greater total TC removal via enhanced adsorption and photocatalytic degradation. In particular, the metallic co-doped photocatalyst (Co/La@g-C_3N_4) displayed a much better adsorptive capacity and photocatalytic activity through the synergy of Co and La dopants on g-C_3N_4 for fast and almost complete TC removal (94% within 30 min). The photocatalytic removal of TC closely follows pseudo-first-order kinetics (Figure 1b; $R^2 \geq 99.0\%$), and the rate constants (k) were calculated: Co/La@g-C_3N_4 (k = 0.28 min^{-1}) > La@g-C_3N_4 (k = 0.25 min^{-1}) > Co@g-C_3N_4 (k = 0.21 min^{-1}) > g-C_3N_4 (k = 0.19 min^{-1}).

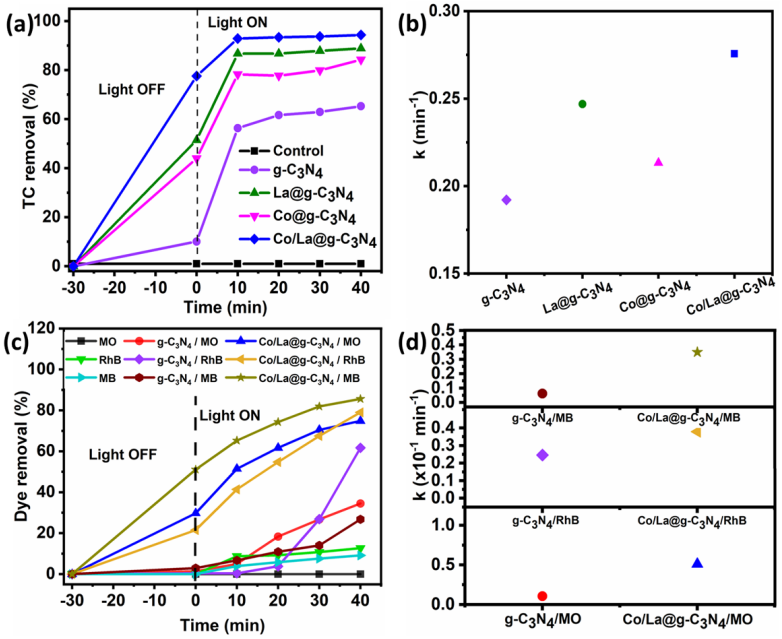

Figure 1. (**a**) TC removal using g-C_3N_4, La@g-C_3N_4, Co@g-C_3N_4, and Co/La@g-C_3N_4 and (**c**) dye removal using g-C_3N_4 and Co/La@g-C_3N_4; (**b**,**d**) corresponding first-order kinetic constants (reaction conditions: temperature = 25 °C, TC concentration = 20 mg L^{-1}, dye concentration = 10 mg L^{-1}, catalyst dosage = 0.4 g L^{-1}, pH_{TC} = 5.05, pH_{MO} = 5.67, pH_{MB} = 3.86, pH_{RhB} = 4.00).

Table 1 shows the competitive photocatalytic TC degradation performance of Co-Co/La@g-C_3N_4 under two TC concentration regimes in comparison with other metal-doped or co-doped g-C_3N_4 photocatalysts reported in the literature. It should be noted that different light sources and reaction conditions (e.g., catalyst dosage, TC concentration, solution pH, and reaction time) were utilized in the literature. However, it is still obvious that our Co/La@g-C_3N_4 shows good photocatalytic activity for fast and high TC removal from water, taking into consideration the selected light source, solution pH, catalyst dosage, TC concentration, and reaction time.

To explore the extended use and universality of the photocatalytic removal of organics by Co/La@g-C_3N_4, three dye targets, i.e., MO, MB, and RhB, as representative anionic, cationic, and zwitterionic dyes, were also tested, as shown in Figure 1c. Significant amounts of the organics were degraded within 40 min of visible-light irradiation, with the highest adsorptive removal in MB solution and the highest rate of degradation in RhB solution. Pristine g-C_3N_4 shows a removal percentage of 35%, 27%, and 62% for MO, MB, and

RhB, respectively. As compared with pristine g-C_3N_4, the total removal % was improved to 75%, 86%, and 79% for MO, MB, and RhB, respectively, attributed to considerably improved adsorption and enhanced photocatalytic degradation (Figure 1c,d). The above results verify that Co/La co-doping into g-C_3N_4 can effectively improve the visible-light photocatalytic activity of g-C_3N_4, and the synthesized Co/La@g-C_3N_4 could potentially be an efficient photocatalyst to treat wastewater containing different organics under visible-light illumination. Moreover, the facile one-pot synthesis of our photocatalyst with good treatment capacity for the removal of various dyes would be advantageous for its practical application in wastewater treatment. To thoroughly explore its applicability and understand the reaction mechanisms, the characterization of the material and its operation optimization were carried out.

Table 1. A comparison of photocatalytic performance for TC removal between Co/La@g-C_3N_4 and other metal-doped or co-doped g-C_3N_4 photocatalysts in the literature.

Photocatalysts (Synthetic Method)	**Dosage (g/L)**	**TC (mg/L)**	**Light Source (Wavelength)**	**Removal (%) within Duration**	**Ref.**
Cu-doped g-C_3N_4 (heating of pre-formed g-C_3N_4 and Cu)	0.2	50	1000 W Xe lamp (λ > 420 nm)	99 (30 min)	[46]
Ba-doped g-C_3N_4 (thermal condensation of $Ba(NO_3)_2$ and melamine)	0.5	10	150 W Xe lamp (λ > 400 nm)	70 (120 min)	[10]
Ag-doped g-C_3N_4 (photodeposition on pre-formed g-C_3N_4)	1.0	20	300 W Xe lamp (λ > 420 nm)	76 (120 min)	[47]
Eu-doped g-C_3N_4 (thermal treatment of pre-formed g-C_3N_4 and Eu_2O_3)	0.2	20	300 W Xe lamp (λ > 420 nm)	82 (50 min)	[12]
La-doped g-C_3N_4 (hydrothermal treatment of pre-formed g-C_3N_4 and $La(NO_3)_3$, followed by calcination)	-	10	Visible light (λ = 400–800 nm)	92 (90 min)	[40]
La_2O_3/g-C_3N_4 (mixing of pre-formed g-C_3N_4 and La_2O_3, followed by drying and heating)	2	20	Visible light (λ ≥ 400 nm)	40 (40 min)	[41]
B/Na co-doped g-C_3N_4 (mixing of pre-formed g-C_3N_4 and sodium borohydride, followed by calcination)	0.1	30	300 W Xe lamp (λ > 420 nm)	78 (30 min)	[14]
B/Eu co-doped g-C_3N_4 (thermal treatment of pre-formed g-C_3N_4, H_3BO_3 and Eu_2O_3)	0.4	20	400 W Halogen lamp	91 (50 min)	[48]
S/Se co-doped g-C_3N_4 (mixing of pre-formed g-C_3N_4 and SeS_2, followed by heating)	0.4	30	500 W Xe lamp (λ > 420 nm)	78 (60 min)	[19]
Co/La@g-C_3N_4 (one-pot synthesis)	0.4	20	300 W Xe lamp (λ > 420 nm)	94 (40 min)	This study
	0.4	50	300 W Xe lamp (λ > 420 nm)	88 (40 min)	

3.2. Mechanism of Enhanced Visible-Light Photocatalytic Activity

3.2.1. Material Property Characterization

In order to better understand the mechanisms governing the enhanced visible-light photocatalytic activity of Co/La@g-C_3N_4, variations in the physicochemical and spectroscopic properties of the synthesized photocatalyst were examined in detail and compared with those of g-C_3N_4, La@g-C_3N_4, and Co@g-C_3N_4.

The FTIR spectra of g-C_3N_4, La@g-C_3N_4, Co@g-C_3N_4, and Co/La@g-C_3N_4 are compared in Figure 2a. All of the photocatalyst samples display similar vibrational patterns [49]. The characteristic band found at 810 cm^{-1} is assigned to the breathing mode of the main structural moiety of g-C_3N_4—the triazine ring. The stretching vibrations of g-C_3N_4 C–N heterocycles are marked by peaks in the range 1210–1650 cm^{-1}. The broad peaks at around 3200 cm^{-1} are attributed to N-H stretching vibration. No noticeable differences are seen in Figure 2a for all photocatalysts; this suggests that the mono-doping or co-doping of g-C_3N_4 herein did not alter the chemical structure of g-C_3N_4, possibly due to the small amounts of dopants introduced.

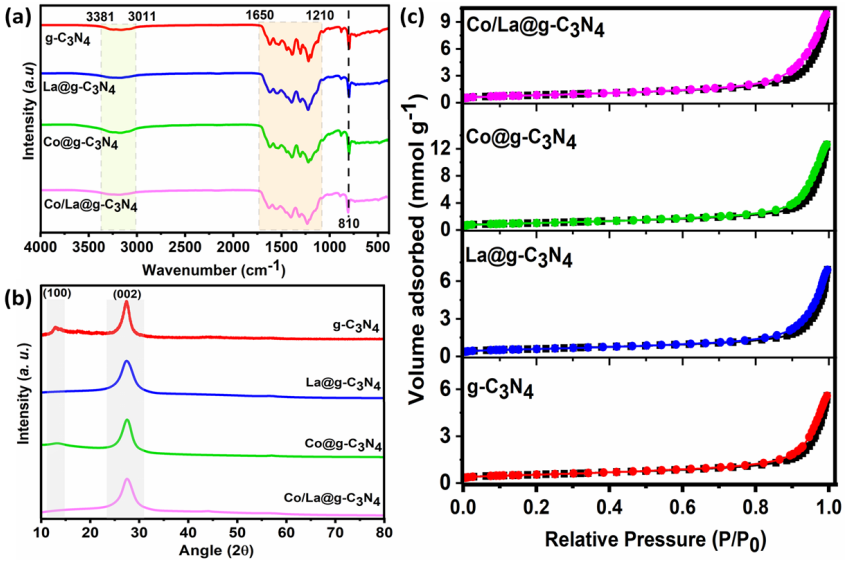

Figure 2. (**a**) FTIR pattern, (**b**) XRD spectra, (**c**) N_2 adsorption–desorption isotherm curves of g-C_3N_4, La@g-C_3N_4, Co@g-C_3N_4, and Co/La@g-C_3N_4.

In Figure 2b, an overall reduction in the intensity of characteristic XRD peaks corresponding to the (100) and (002) crystal planes of g-C_3N_4 is observed for all doped g-C_3N_4. Specifically, the peak at 13.1°, indexed to the (100) facet and ascribed to the in-plane repeating tris-s-triazine units, diminishes upon doping [50]. Smaller crystallite sizes, calculated using the Scherrer equation, are shown in Table 2 for all doped g-C_3N_4 variants. These suggest that the introduction of metal dopants interferes with the thermal polymerization of precursors forming g-C_3N_4 and then leads to a reduction in the ordered structure in the framework [51]. There are no apparent new peaks associated with Co or La species in any of the doped g-C_3N_4 variants, which might be explained by the small amounts of dopants added.

Table 2. Crystalline sizes and textural properties (pore diameter, pore volume, and BET specific surface area) of g-C_3N_4, La@g-C_3N_4, Co@g-C_3N_4, and Co/La@g-C_3N_4.

Photocatalyst	Crystalline Size (nm)	Pore Diameter (nm)	Pore Volume ($cm^3\ g^{-1}$)	Specific Surface Area ($m^2\ g^{-1}$)
g-C_3N_4	4.77	18.6	0.0124	41.3
La@g-C_3N_4	2.02	20.5	0.0135	45.8
Co@g-C_3N_4	2.57	20.9	0.0241	79.8
Co/La@g-C_3N_4	2.08	19.2	0.0192	65.5

The textural properties, including porosity and BET specific surface area, of various samples are detailed and summarized in Table 2; their nitrogen adsorption–desorption isotherm curves are included in Figure 2c. All of the samples display typical IV isotherm

curves and H3-hysteresis loops, suggesting the presence of silt-like mesopores [52]. Overall, Co- or/and La-doped g-C_3N_4 exhibited increases in pore volume, pore diameter, and BET specific surface area with respect to g-C_3N_4, which could be due to the altered polymerization of urea in the presence of different metal dopants. Such features might be beneficial in promoting the transport of pollutants into photocatalyst pores and then their arrival at active sites for reactions. The sample of Co@g-C_3N_4 displayed the most significant increase in BET specific surface area (79.8 m^2 g^{-1}) as compared to g-C_3N_4 (41.3 m^2 g^{-1}). The increase in the surface area of Co@g-C_3N_4 may be ascribed to the creation of porous structures induced by co-doping during polymerization [53]. This is also reflected in the increase in the pore diameter and pore volume (20.9 nm and 0.0241 cm^3 g^{-1} for Co@g-C_3N_4 vs. 18.6 nm and 0.0124 cm^3 g^{-1} for g-C_3N_4). The surface area and pore volume of La@g-C_3N_4 are comparable to those of g-C_3N_4, but they show a slightly larger average pore diameter. The reduced pore diameter of the co-doped photocatalyst (Co/La@g-C_3N_4) compared to the mono-doped samples (La@g-C_3N_4 or Co@g-C_3N_4) could be due to the pore and channel obstruction by the dopants [54].

The morphology of g-C_3N_4, as shown in Figure 3a, is characterized by the stacked non-uniform sheet-like morphology of g-C_3N_4, which ensued from the thermal polymerization of urea. Upon doping with Co and La, a graphitic-like morphology with non-uniform sheets and obvious porosity is observed in the modified sample, which are believed to be advantageous features for the photocatalytic degradation of organic pollutants.

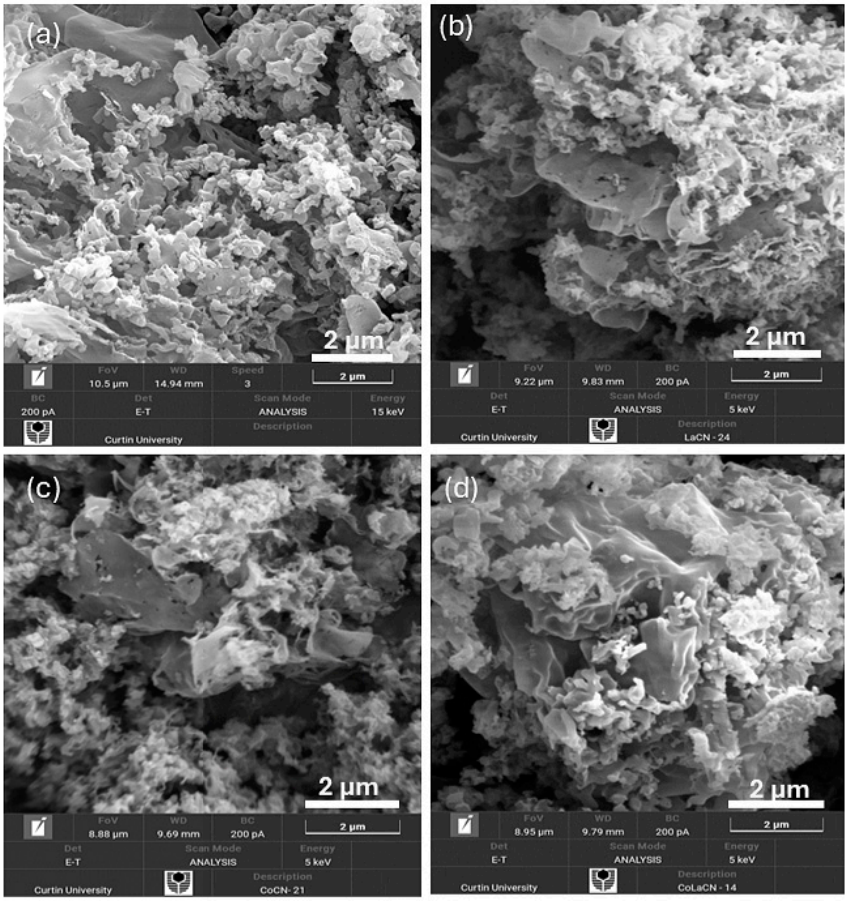

Figure 3. SEM images of (**a**) g-C_3N_4, (**b**) La@g-C_3N_4, (**c**) Co@g-C_3N_4, and (**d**) Co/La@g-C_3N_4.

Figure 4 details the microstructure of Co/La@g-C_3N_4, with a typical lamellar structure (Figure 4a) and the distribution of dopant particles on it (Figure 4b). The HRTEM images (Figure 4c,d) show lattice fringes with a spacing of 0.15 nm and 0.29 nm, corresponding to the (511) and (011) planes of Co_3O_4 and La_2O_3, respectively [55,56]. The high-angle

annular dark-field (HAADF) image (Figure 4e) confirms the presence of C, N, O, Co, and La in Co/La@g-C_3N_4; the distribution of each constituent element is presented in Figure 4e-i–e-v. It is noteworthy that the detected O atom was incorporated during the thermal polymerization of urea [57]. TEM and SEM observations indicate that upon the introduction of Co and La, Co_3O_4 and La_2O_3 grow on the surface of g-C_3N_4, forming a p-n-p heterojunction and later showing improved photocatalytic activity for pollutant removal.

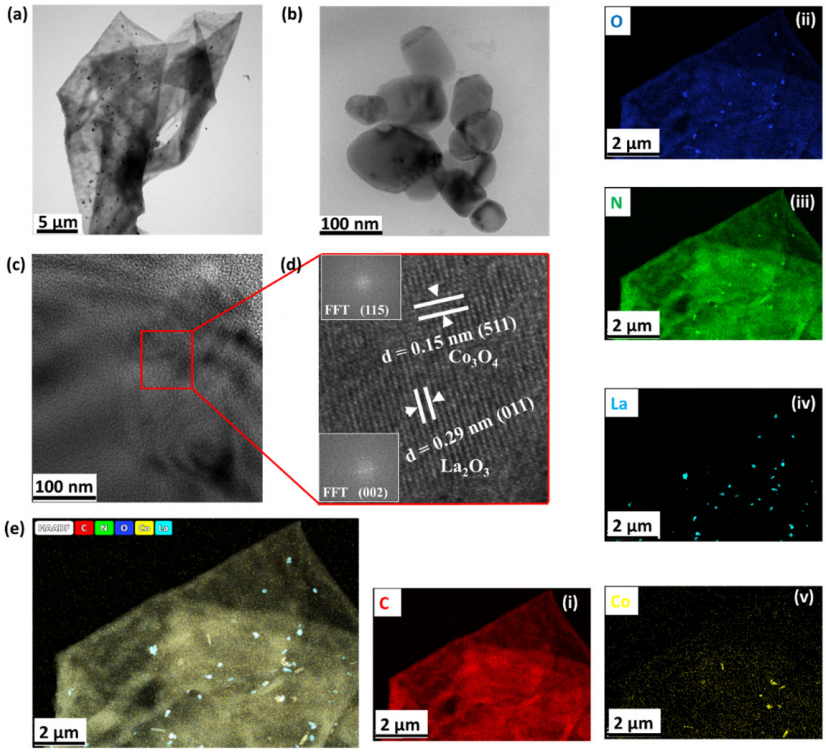

Figure 4. TEM images (**a**,**b**), HRTEM images (**c**,**d**), and HAADF images of elemental mapping ((**e-i**): C; (**e-ii**): O; (**e-iii**): N; (**e-iv**): La; (**e-v**): Co; (**e**): all above elements) of Co/La@g-C_3N_4.

The XPS survey spectrum (Figure 5a) shows signals of N, O, and C, along with Co and La. The deconvoluted C 1s spectrum shows three main peaks at 284.5 eV, 287.8 eV, and 290.3 eV, which are attributed to adventitious C-C/C=C, -C-N/-C=N, and -O-C=N functional groups, respectively (Figure 5b) [58,59]. The deconvolution of the N 1s spectrum resulted in three peaks at binding energies of 399.1 eV, 401.4 eV, and 403.7 eV, which are ascribed to the nitrogen atoms of C=N-C, N-$(C)_3$, and C-NH_2, respectively (Figure 5c) [60]. The XPS spectra of O 1s with two peaks at binding energies of 532.5 eV and 536.6 eV suggest oxygen atoms in C-O and loosely bonded oxygen species on the surface, e.g., adsorbed water molecules (Figure 5d) [61]. The XPS spectrum of Co 2p can be deconvoluted into Co $2p_{3/2}$ and Co $2p_{1/2}$ with binding energies (satellite peaks) of 779.5 eV (sat. 786.9 eV) and 794.1 eV (sat. 803.7 eV), respectively (Figure 5e), suggesting the presence of Co^{2+} and Co^{3+} [62,63]. The XPS spectrum of La 3d revealed two peaks at 840.0 eV and 857.1 eV, which are attributed to La $3d_{5/2}$ and La $3d_{3/2}$, respectively (Figure 5f). The spin–orbit coupling between these two peaks was calculated to be 17.1 eV, which is similar to other reported work [55]. Our XPS results further support the successful co-doping of La and Co into g-C_3N_4 in the sample of Co/La@g-C_3N_4, which was observed in the above TEM and EDX images.

Figure 6a reveals an increase in visible-light absorption in the samples of La@g-C_3N_4, Co@g-C_3N_4, and Co/La@g-C_3N_4 as compared to the parent g-C_3N_4, with an absorption band edge around 465 nm. The samples of Co@g-C_3N_4 and Co/La@g-C_3N_4 exhibited a further shift in absorption to about 600 nm. The extra absorption shoulder, especially exhibited by Co/La@g-C_3N_4, in the far-visible region might be ascribed to n–π^* transitions

in the conjugated system of g-C_3N_4 when the structural distortion was developed [64]. The improved absorption in the visible-light range might also be due to the synergistic effect of the two dopants and g-C_3N_4. The band gaps (E_g) of the parent g-C_3N_4, La@g-C_3N_4, Co@g-C_3N_4, and Co/La@g-C_3N_4 were measured by adopting the Kubelka–Munk equation and are shown in Figure 6b, with values of 2.74 eV, 2.60 eV, 2.50 eV, and 2.62 eV, respectively.

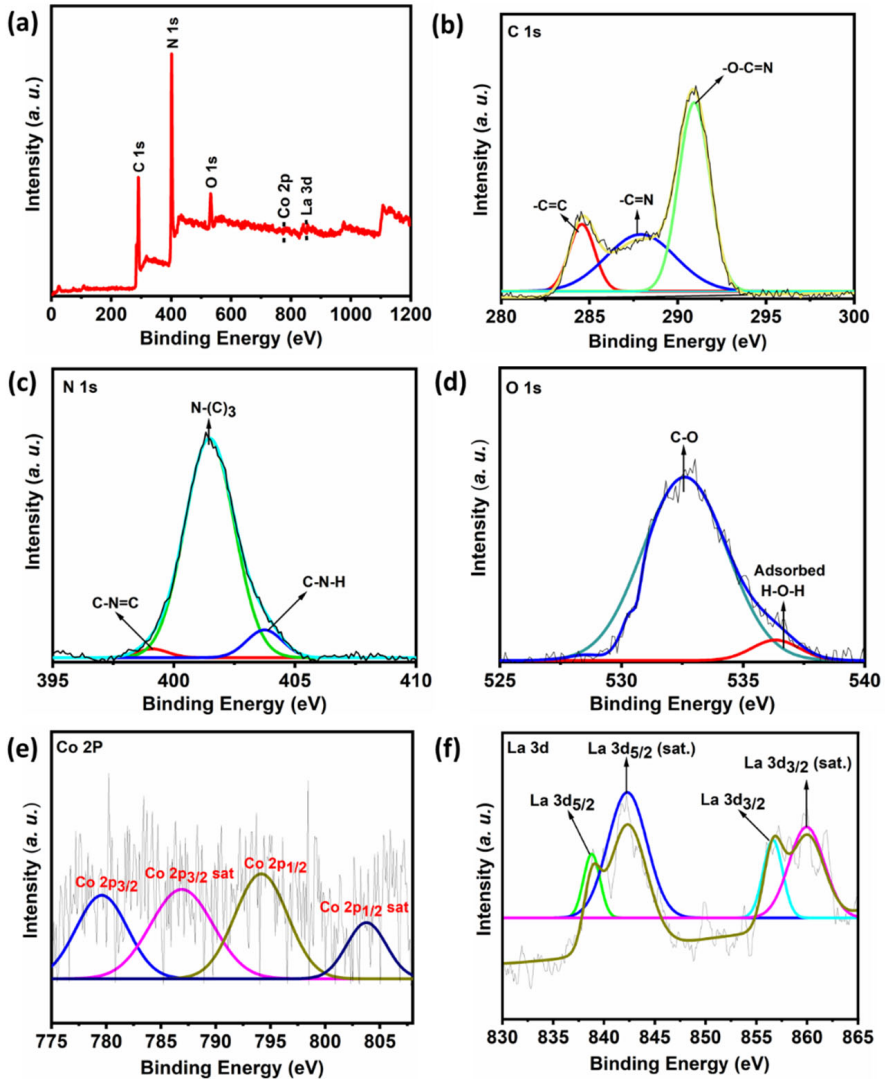

Figure 5. XPS spectra of Co/La@g-C_3N_4: (**a**) survey spectrum; (**b**) C 1s, (**c**) N 1s, (**d**) O 1s, (**e**) Co 2p, and (**f**) La 3d.

The photocurrent response and electrochemical impedance spectroscopy (EIS) data were collected to investigate the separation and transfer of photogenerated charge carriers over our as-prepared photocatalysts. Figure 6c shows the order of the photocurrent density: g-C_3N_4 < Co@g-C_3N_4 < La@g-C_3N_4 < Co/La@g-C_3N_4. In particular, the photocurrent density of Co/La@g-C_3N_4 increases rapidly and is much higher than that of the parent g-C_3N_4, indicating that the synergistic effect of co-doped Co and La on g-C_3N_4 results in the fast separation of photogenerated charge carriers. The EIS Nyquist plots (in Figure 6d) suggest the charge transfer resistance of the photocatalysts; generally, a smaller arc radius represents a lower interfacial transfer resistance and greater electron mobility. As compared with g-C_3N_4, the interface resistance of Co/La@g-C_3N_4 is reduced by the synergistic interaction between dopants and g-C_3N_4, which promotes charge separation and, in turn, enhances photocatalytic degradation performance.

The pristine g-C_3N_4 and Co/La@g-C_3N_4 band-edge potentials were determined from the Mott–Schottky analysis at different frequencies (100 Hz, 500 Hz, and 1000 Hz). The positive slopes in the Mott–Schottky plots of both samples suggest n-type semiconductor features [65]. By extrapolating $1/C^2 = 0$ in the plots (Figure 6e,d), the flat-band potentials of g-C_3N_4 and Co/La@g-C_3N_4 were deduced to be −0.64 eV and −0.50 eV (vs. Ag/AgCl electrode), respectively. In general, the flat-band potential is approximately equal to the conduction band potential (E_{CB}), and it is 0.1 eV more negative than the band potential for n-type semiconductors [66,67]. Thus, the E_{CB} values of g-C_3N_4 and Co/La@g-C_3N_4 are −0.74 eV and −0.60 eV, equivalent to −0.54 eV and −0.40 eV versus the normal hydrogen electrode (i.e., E_{NHE} = Ag/AgCl + 0.197). The valence band potentials (E_{VB}) of g-C_3N_4 and Co/La@g-C_3N_4 were calculated to be +2.20 eV and +2.22 eV, respectively, using the equation $E_{VB} = E_{CB} + E_g$ [21]. The following results indicate a band gap narrowing with a positive shift in E_{CB} and E_{VB} edges of g-C_3N_4 upon co-doping with Co and La.

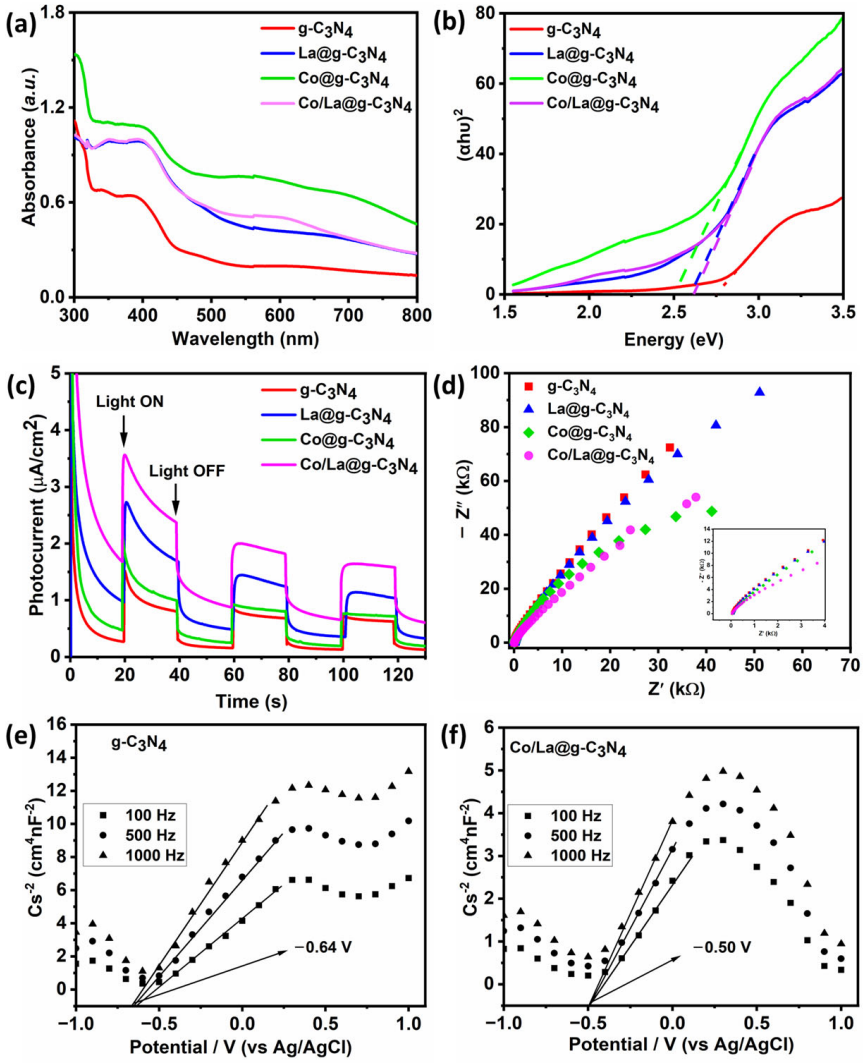

Figure 6. (**a**) UV-Vis DRS, (**b**) $(\alpha h\nu)^2$ vs. hν plots, (**c**) transient photocurrent response curves, and (**d**) EIS Nyquist plots of g-C_3N_4, La@g-C_3N_4, Co@g-C_3N_4, and Co/La@g-C_3N_4; (**e**,**f**) Mott–Schottky plots of g-C_3N_4 and Co/La@g-C_3N_4.

3.2.2. Routes of Active Species Formation and Possible Pathways of Degradation

To identify active species involved in the photocatalytic degradation of TC over Co/La@g-C_3N_4, reagents, including BQ, IPA, Na_2EDTA, L-Trp., and $AgNO_3$, were utilized to scavenge superoxide radicals ($\bullet O_2^-$), hydroxyl radicals (•OH), holes (h^+), singlet oxygen

($^1O_2$), and electrons (e^-), respectively. Figure 7a compares the removal of TC in the presence of different scavenging agents against the control in the absence of any agent. When IPA is introduced as a capture agent, the removal of TC is slightly impeded, indicating a minor role of •OH during the degradation reaction. The TC removal percentage is reduced to about 53% when Na_2EDTA is added, showing an important role of h^+ in the overall photocatalytic degradation. The lowest TC removal % (13%) is noticed upon adding BQ, suggesting $•O_2^-$ as the main ROS responsible for the removal of TC over Co/La@g-C_3N_4. The presence of $^1O_2$ is deduced via the retarding of the TC removal effect of the L-Trp. reagent. The coexistence of $^1O_2$ in the photocatalytic reaction system may be associated with the h^+-induced oxidation of $•O_2^-$ [68]. The synergy in generating electrons by the co-doped La and Co atoms was examined by introducing $AgNO_3$ as a capture agent. Only about 1% of TC was degraded when the photogenerated e^- was captured by $AgNO_3$, showing the important role of e^- in the generation of the main ROS ($•O_2^-$).

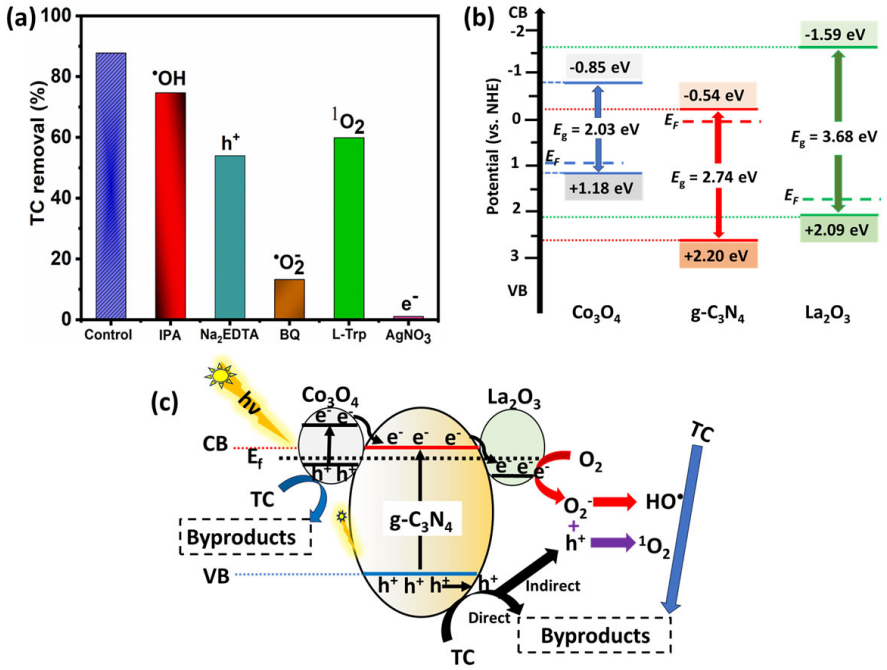

Figure 7. (**a**) Experimental determination of reactive species (reaction conditions: temperature = 25 °C, TC concentration= 50 mg L^{-1}, dosage = 0.4 g L^{-1}, and pH_{TC} = 5.05), (**b**) electronic energy bands of Co_3O_4, g-C_3N_4, and La_2O_3 before contact, and (**c**) schematic representation of photocatalytic degradation mechanism of Co/La@g-C_3N_4.

Based on the above scavenging experiment, the TEM microstructure, and electronic band potential edges of Co/La@g-C_3N_4, a possible degradation mechanism is proposed (Figure 7c). The as-prepared photocatalyst was shown earlier to consist of Co_3O_4 and La_2O_3 on the surface of g-C_3N_4. g-C_3N_4 is an n-type semiconductor, whilst both Co_3O_4 and La_2O_3 are p-type semiconductors [63,69]. With the newly constructed Co/La@g-C_3N_4 ternary composite photocatalyst, a p-n-p heterojunction is formed among g-C_3N_4 and the two types of metal oxides.

For a concise understanding of the heterojunction formation with g-C_3N_4, the electronic band structures of the metal oxides were investigated using UV-Vis DRS and Mott–Schottky analysis. The band gap (Figures S2 and S3) and conduction band (CB) from the Mott–Schottky plots (Figures S4 and S5) of Co_3O_4 and La_2O_3 were measured to be 2.03 eV (VB = +0.99 V (+1.18 eV vs NHE)) and 3.68 eV (VB = +1.90 V (+2.09 eV vs NHE)), respectively. The corresponding valence bands (CBs) of Co_3O_4 and La_2O_3 were separately computed to be -0.85 eV and -1.59 eV. The band-edge potentials of the respective semiconductors before contact are shown in Figure 7b. The Fermi level (E_F) of Co_3O_4 or La_2O_3 is

located just above the VB top for p-type semiconducting materials, whilst that of g-C_3N_4 is situated just below the CB bottom. In the p-n-p junction formation and Fermi level equilibration, holes are migrated from the VB of the p-type semiconductors (Co_3O_4 and La_2O_3) to CB of the n-type semiconductor (g-C_3N_4) because of concentration differences [67]. At the same time, electrons diffuse from the CB of g-C_3N_4 to the CB of (Co_3O_4 and La_2O_3), giving rise a positively charged g-C_3N_4 and negatively charged (Co_3O_4 and La_2O_3). As reported in the literature, an internal electric field forms between g-C_3N_4 and metal oxides in the Fermi level equilibration of p-type and n-type semiconductors, resulting in a shift in their band positions [70]. As shown in Figure 7c, the energy bands of metal oxides shift upward along the Fermi levels; the energy bands of g-C_3N_4 shift downward along the Fermi levels. Following visible-light irradiation, photogenerated electrons are excited to the respective CBs of the two visible-light-responsive semiconductors (g-C_3N_4 and Co_3O_4), leaving holes in the VBs (Figure 7c). Electrons are transferred from the CB of p-type Co_3O_4 to n-type g-C_3N_4 and holes migrate in the reverse direction. Additionally, the co-doping of Co and La aided the separation of the photogenerated charge carriers and minimized the charge transfer resistance of the photocatalyst, as observed in Figure 6c,d. On the other side, La_2O_3, as a visible-light-inactive metal oxide, cannot be excited under visible-light illumination due to its large band gap. At the junction interface of g-C_3N_4 and Co_3O_4, electrons are diffused from the CB of Co_3O_4, which is more negative, to the CB of g-C_3N_4, leaving holes in the VB for the direct oxidation of TC molecules into their smaller byproducts. Consequently, the accumulated electrons in the CB of g-C_3N_4 are transferred to the surface of a visible-light-inactive La_2O_3, where they react with dissolved oxygen in the aqueous solution to generate $\bullet O_2^-$ (as evidenced in Figure 7a). Most organic pollutants are not degraded directly by $\bullet O_2^-$ due to its low oxidation potential. Thus, it is transformed into stronger oxidants like •OH and $^1O_2$ by reacting with water and holes, respectively, which are utilized for TC degradation [71]. The synergistic effect among g-C_3N_4, Co_3O_4, and La_2O_3 facilitates electron separation and transfer in the ternary nanocomposite and, in turn, results in the accumulation of electrons on the photocatalyst surface, as deduced from the scavenging test when using $AgNO_3$ as an agent to capture electrons (Figure 7a). The tertiary Co_2O_3/g-C_3N_4/La_2O_3 in Co/La@g-C_3N_4 plays a vital role in boosting the photocatalytic activity of the catalyst.

Plausible pathways are proposed for TC degradation using the as-prepared Co/La@g-C_3N_4, as shown in Figure 8. The TC molecule (in Figure 8) structurally consists of various ionizable functional and high-electron-density groups, such as phenol, amino, and conjugated double bonds. It is prone to be attacked by reactive species—$\bullet O_2^-$, $^1O_2$, •OH, or h^+, which were proven to be present in the scavenging test (Figure 7a)—to generate the identified intermediates—peaks P1–P11 with m/z consistent with the literature [72–75], as shown in the LC–MS analysis (Figure S6). It is noteworthy that since the main ROS, $\bullet O_2^-$, has a lower oxidation potential than most organic pollutants, it may be converted to •OH or $^1O_2$ species with a stronger oxidation potential for degrading TC molecules [71]. Based on the literature [71–78] and the identified main ROS ($\bullet O_2^-$), we propose two degradation routes, as illustrated in Figure 8. In pathway I, a primary intermediate (P1) with m/z = 476.45 can be generated through hydroxylation at C-11a and C-2 of the TC molecule (m/z = 445.25) [76]. Subsequently, P1 may be fragmented into P2 (m/z = 453.15) via dehydroxylation, and a further loss of the hydroxyl group at C-6 could produce P3 (m/z = 425.20). The peak P4 (m/z = 339.05) may be obtained from P3 via demethylation, dehydroxylation, and deamination [74]. The subsequent demethylation of P4 could transform it into P5 (m/z = 308.30) [77]. In pathway II, the TC molecule could be directly attacked to produce P7 (m/z = 400.00) via a deacylation reaction at C-1 and C2 of the TC molecule and further fragment to give P6 (m/z = 263.05) [72]. The intermediates P5 and P6, due to continuous attack by the ROS, could fragment into a series of lower-molecular-weight intermediates, including P8 (m/z = 165.95), P9 (m/z = 149.95), P10 (m/z = 128.10), P11 (m/z = 105.05), CO_2, and water molecules, through ring opening and molecular rearrangement [78].

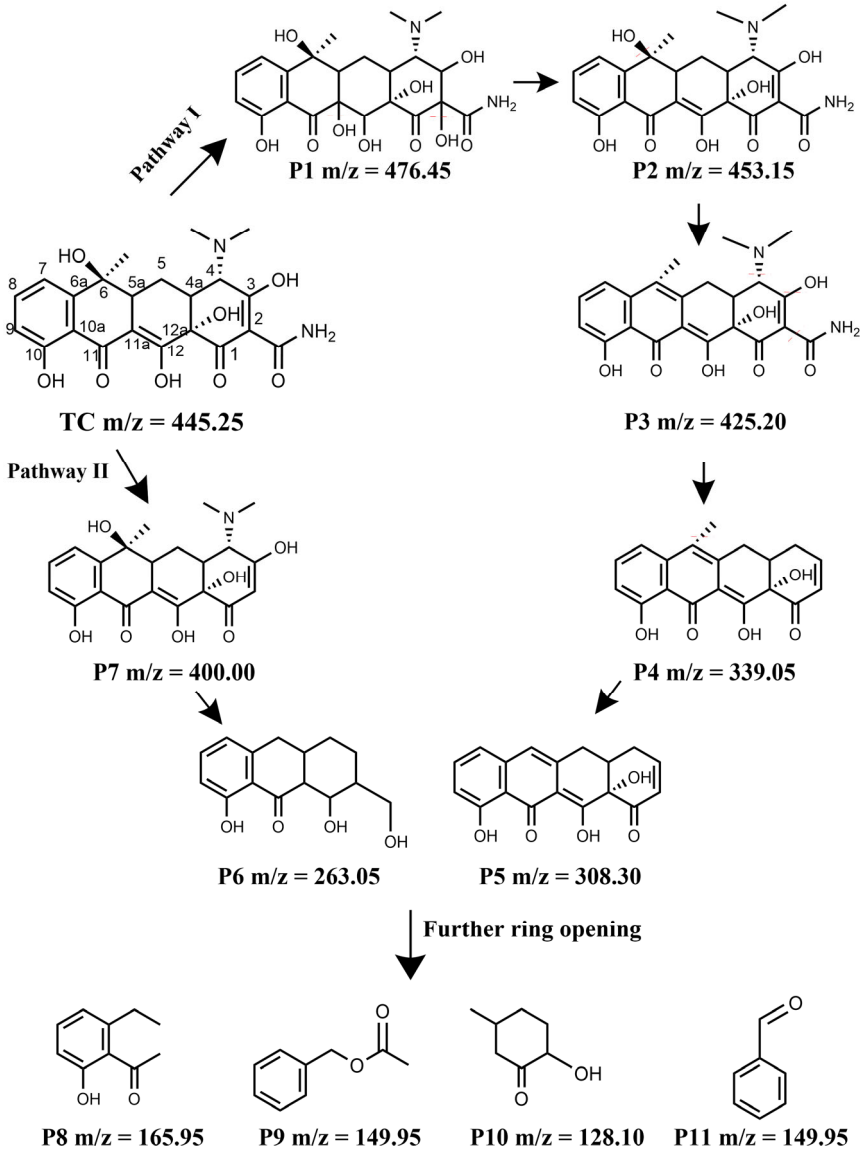

Figure 8. Plausible routes for the degradation of TC using Co/La@g-C_3N_4.

3.3. Effects of Reaction Conditions on Photocatalytic Degradation

Figure 9a shows the effect of the catalyst dosage (0.1 g L^{-1}–0.6 g L^{-1}) on TC removal using Co/La@g-C_3N_4. TC removal increases from 80% at a dosage of 0.1 g L^{-1} to 88% at a dosage of 0.4 g L^{-1}. The improvement in photocatalytic performance, which is evident from the higher rate constants with greater sample loading, may be due to the increasing number of exposed active sites on the photocatalyst for the adsorption of TC and the absorption of light, as well as the generation of reactive species for photocatalytic TC degradation [79]. On the other side, excessive loading (e.g., at a dosage of 0.6 g L^{-1}) results in a decline in the removal rate of TC (80%), which is believed to be associated with greater turbidity of the solution, preventing light penetration through aqueous media [80]. Furthermore, a high catalyst dosage may lead to the agglomeration of photocatalyst particles, the reduced availability of active sites on the catalyst surface, and, eventually, a decrease in the number of reactive species for the photocatalytic reaction [79,80]. As can be seen from our results, a dosage of 0.4 g L^{-1} was suggested as the optimal dose for photocatalytic TC degradation over Co/La@g-C_3N_4 in subsequent experiments.

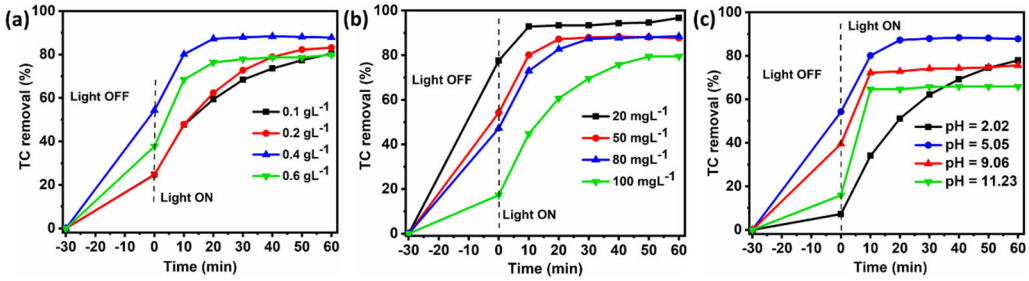

Figure 9. The impact of factors on the removal of TC using Co/La@g-C_3N_4: (**a**) photocatalyst dosage; (**b**) initial TC concentration; (**c**) solution pH (reaction conditions if not specified otherwise: temperature = 25 °C, TC concentration = 50 mg L^{-1}, dosage = 0.4 g L^{-1}, and pH_{TC} = 5.05).

The initial TC concentration was varied from 20 mg L^{-1} to 100 mg L^{-1} to study the impact of pollutant concentration on its removal (Figure 9b). Prior to light illumination, the adsorption in the dark decreases with increasing TC concentration, which may be due to the excessive number of adsorbates on catalyst adsorptive sites [81]. Upon illumination, the photocatalytic removal of TC over Co/La@g-C_3N_4 varies with the initial TC concentration, especially within the first 20 min of the reaction. The value of k is higher at lower concentrations of TC, e.g., 20 mg L^{-1} TC (0.28 min^{-1}), as compared with 50 mg L^{-1} TC (0.15 min^{-1}), 80 mg L^{-1} TC (0.10 min^{-1}), and 100 mg L^{-1} TC (0.05 min^{-1}). This decline in the photocatalytic performance of Co/La@g-C_3N_4 may be due to the occupation of active sites by an excessive amount of TC (or produced intermediate products) and then the reduced formation of reactive species and photocatalysis reaction [82,83]. Moreover, the absorption of light by a greater amount of TC or its intermediates in the solution would hinder photon absorption on the catalyst active sites and, in turn, might deteriorate the photocatalytic activity of Co/La@g-C_3N_4 [79]. As can be seen, the increase in the initial TC concentration from 20 mg L^{-1} to 100 mg L^{-1} results in a corresponding decrease in TC removal from 88% to 73%, which aligns with the literature [79].

The solution pH is an important factor for optimizing photocatalytic degradation, as it affects the surface charge of the catalyst and the ionic form of the pollutant [84]. Figure 9c shows the removal of TC using Co/La@g-C_3N_4 at different pHs. The highest adsorption in the dark is recorded at pH = 5.05, whilst the highest rate constant (k) is found at pH = 11.23 (k = 0.35 min^{-1}). An optimal total TC removal of 88% is observed at pH = 5.05. A further increase in pH resulted in a corresponding decrease in the removal of TC from 76% (pH = 9.06) to 66% (pH = 11.23). The point of zero charge (PZC) of Co/La@g-C_3N_4 is shown in Figure S1, 6.6. This implies that at pH > pH_{PZC}, the catalyst surface is negatively charged, whilst at pH < pH_{PZC}, it gives rise to a positively charged surface. It is known that TC molecules exist in dissimilar forms depending upon the pH of the solution [85], including cationic species (pH < 3.3), zwitterionic species (3.3 < pH < 7.68), or anionic species (pH > 7.68). In our study herein, as compared with lower pH, the faster degradation rate at higher pH might be ascribed to the unstable nature of TC in alkaline conditions [86]. Meanwhile, at higher pH, the electrostatic repulsion between the negatively charged surface of the catalyst and the anionic form of TC molecules, as well as the competition between hydroxide ions and pollutants for active sites of the catalyst, might both contribute to the observed lower adsorption in the dark and then overall TC removal [86]. On the other side, acidic conditions (e.g., pH = 2.02) are not favourable for the adsorption of the cationic form of TC molecules onto the positively charged catalyst surface due to electrostatic repulsion [87]. Thus, lower adsorptive removal and the subsequent photocatalytic degradation of TC are seen when using Co/La@g-C_3N_4.

Organic pollutants are usually found to exist with many foreign ions in wastewater or water. Figure 10a shows the specific removal of TC using Co/La@g-C_3N_4 in the presence of some of the most common ions (e.g., Cl^-, SO_4^{2-}, or NO_3^-). As compared with the control (in the absence of foreign ions), the adsorptive and photocatalytic removal of Co/La@g-C_3N_4 is noticed to vary insignificantly (~5% variation). The order of k change is NO_3^-

($k = 0.22\ min^{-1}$) > Cl^- ($k = 0.17\ min^{-1}$) > SO_4^{2-} ($k = 0.16\ min^{-1}$), relative to the control ($k = 0.15\ min^{-1}$). A plausible explanation for this phenomenon may be attributed to the possible formation of the radicals Cl•, NO_3•, and SO_4^- in the presence of the corresponding inorganic ions [84,88]. Our results demonstrate the robustness of Co/La@g-C_3N_4 for the efficient removal of TC in the presence of different inorganic ions.

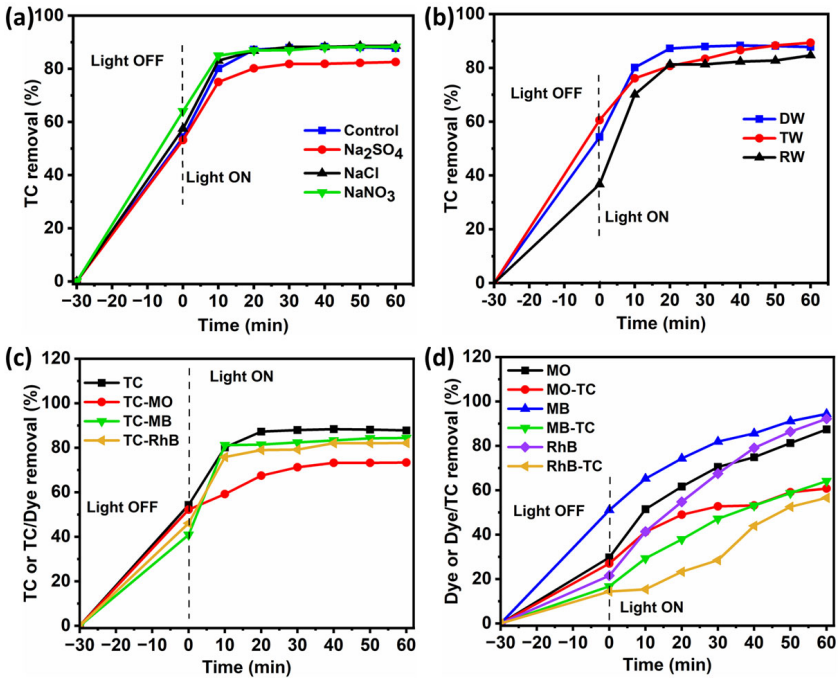

Figure 10. The impact of factors on the removal of TC using Co/La@g-C_3N_4: (**a**) counter ions; (**b**) water matrices; (**c**,**d**) binary systems (reaction conditions if not specified otherwise: temperature = 25 °C, TC concentration = 50 mg L^{-1}, dye concentration = 10 mg L^{-1}, catalyst dosage = 0.4 g L^{-1}, pH_{TC} = 5.05, pH_{MO} = 6.00, $pH_{TC/MO}$ = 4.72, pH_{MB} = 3.86, $pH_{TC/MB}$ = 4.53, pH_{RhB} = 4.00, and $pH_{TC/RhB}$ = 4.03).

Figure 10b compares TC removal using Co/La@g-C_3N_4 from different water matrices: deionized water (DW), rainwater (RW), and tap water (TW). As compared with TW and DW, lower adsorption of TC in the dark but greater photocatalytic removal of TC is seen in RW. The total TC removal changed insignificantly, which was 89% in TW, 88% in DW, and 85% in RW. The rate constant of degradation (k) is in the increasing order TW ($0.09\ min^{-1}$) < RW ($0.11\ min^{-1}$) < DW ($0.15\ min^{-1}$). Figure S7 shows the total removal of TC from the primary (PWW) and secondary effluents (SWW), which were collected from a Perth local municipal wastewater treatment plant, reaching ~80% and 75% after 30 min adsorption and 60 min visible-light photocatalytic degradation, respectively. In general, our prepared Co/La@g-C_3N_4 exhibited good photodegradation activity in various water matrices.

Organic pollutants always exist along with other pollutants in real wastewater. Figure 10c investigates the versatility of Co/La@g-C_3N_4 in a binary solution consisting of TC and different dyes (e.g., MO, MB, and RhB). The total TC removal using Co/La@g-C_3N_4 decreases to about 73%, 84%, and 82% in binary mixtures of TC/MO, TC/MB, and TC/RhB, respectively, as compared to the TC-only solution (88%). The values of k for photocatalytic TC degradation in the systems of TC/MO, TC/RhB, and TC/MB are $0.05\ min^{-1}$, $0.18\ min^{-1}$, and $0.30\ min^{-1}$, respectively, in comparison with $0.15\ min^{-1}$ in the TC-only system. The reduced removal of TC and dyes from the binary systems, in comparison with the dye-only solution systems, could be due to competition for the adsorptive sites of Co/La@g-C_3N_4 [89]. Additionally, the effect of binary systems on the removal of dye/TC mixtures as compared to the dye-only solutions was investigated (Figure 10d). The significant removal

performance of all dye-only solutions is noticed after 60 min of visible-light illumination. However, the degradation % of the respective dye is impeded in a binary system, which could be due to the electrostatic interactions between various ionic species of TC and the dye molecules. In the dark reaction, a decrease in adsorption can be observed in dye/TC binary systems relative to the dye-only solution, which affects the overall removal performance of the dye molecules. The rate of TC removal can also be affected by hydrogen bonding between the dyes and TC molecules and their electrostatic interactions with the surface of Co/La@g-C_3N_4 [90].

Relatively good reusability of Co/La@g-C_3N_4 can be achieved with five cycles of photocatalytic TC degradation, during which the degradation rate is reduced by less than 10%, as shown in Figure 11a. The stability of Co/La@g-C_3N_4 in the reaction is supported by the almost unchanged XRD patterns and FTIR spectra of fresh Co/La@g-C_3N_4 and spent Co/La@g-C_3N_4 (after fifth cycle of use), respectively. The ICP-AES analysis shows negligible amounts of Co (0.84 mg/kg) and La (2.8 mg/kg) in the solution after the photocatalytic reaction, which suggests that approximately 0.02% and 0.01% of the actual amount of Co (4500 mg/kg) and La (28,000 mg/kg) dopants leach out into the solution from the photocatalyst. This further proves the stability of Co/La@g-C_3N_4 for recycling and reuse.

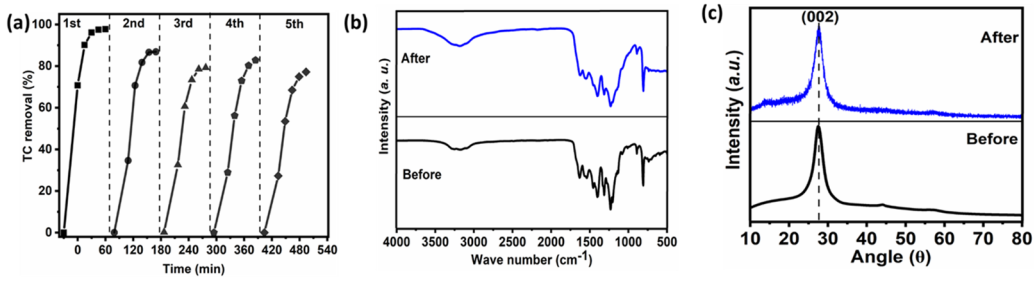

Figure 11. (**a**) The reusability of Co/La@g-C_3N_4 for photocatalytic TC degradation, (**b**) FTIR spectra, and (**c**) XRD patterns of fresh and spent Co/La@g-C_3N_4 (after the 5th run). (Reaction conditions: temperature = 25 °C, concentration of TC = 20 mg L^{-1}, catalyst dosage= 0.4 g L^{-1}, pH_{Tc} = 5.05).

4. Conclusions

A facile one-pot pyrolysis method was utilized by mixing urea and Co- and La-containing precursors to synthesize a g-C_3N_4-based ternary photocatalyst (Co/La@g-C_3N_4) with a unique p-n-p heterojunction. Upon visible-light illumination, Co/La@g-C_3N_4 displayed improved performance, achieving 94% TC removal, as compared with 65% of the pristine g-C_3N_4. The enhanced photocatalytic activity of Co/La@g-C_3N_4 was ascribed to the improved photogenerated charge separation, reduced charge transfer resistance, built-in electric energy arising from the p-n-p heterojunction, and synergistic effect of ternary components for the generation and transfer of electrons. Additionally, Co/La@g-C_3N_4 showed excellent performance under varying reaction conditions, including the solution pH, catalyst dosage, TC concentration, co-existing ion, and water matrix. Photocatalytic TC degradation by Co/La@g-C_3N_4 could be largely maintained after the fifth cycle of the reaction, confirming its good stability and reusability. The capture experiment demonstrated that $\bullet O_2^-$ played the most important role in the photocatalytic reaction. The facile fabrication and high performance of the Co/La@g-C_3N_4 ternary nanocomposite in this work suggest the promising potential for its practical application as a highly efficient visible-light-active photocatalyst.

Supplementary Materials: The following supporting information can be downloaded at: https://www.mdpi.com/article/10.3390/w16182563/s1, Table S1: Physical parameters of different water matrices: DW, RW, and TW; Figure S1: Point of zero charge (PZC) of Co/La@g-C_3N_4; Figure S2: UV-Vis DRS and $(\alpha h\nu)_2$ vs. hν plots (inset) of Co_3O_4; Figure S3: UV-Vis DRS and $(\alpha h\nu)_2$ vs. hν plots (inset) of La_2O_3; Figure S4: Mott-Schottky plot of Co_3O_4; Figure S5: Mott-Schottky plot of La_2O_3; Figure S6: MS spectra for the intermediates of TC after photocatalytic treatment (i) 0 min, (ii) 20 min, and (iii) 60 min (reaction conditions: temperature = 25 °C; concentration of TC = 10 mg/L M; Co/La@g-C_3N_4 = 0.4 g L^{-1}; pH TC = 5.05); Figure S7: Removal of TC using Co/La@ g-C_3N_4 in the primary effluent (PWW) and secondary effluent (SWW).

Author Contributions: Conceptualization, K.I.J. and D.L.; methodology, K.I.J. and D.L.; formal analysis, K.I.J. and T.B.I.; investigation, K.I.J. and T.B.I.; writing—original draft preparation, K.I.J.; writing—review and editing, K.I.J., T.B.I., G.H., A.N.N. and D.L.; supervision, G.H. and D.L.; funding acquisition, D.L. All authors have read and agreed to the published version of the manuscript.

Funding: This research was partially funded by SHEE Small Research Grant at Murdoch University. It received no external funding.

Data Availability Statement: Data are available on request due to restrictions.

Acknowledgments: The authors acknowledge Juita Juita and Malgorzata Kowalczyk for their training and discussion on the analysis. The authors acknowledge the use of equipment and scientific and technical assistance of the Curtin University Electron Microscope Facility and the help from Elaine Miller.

Conflicts of Interest: The authors declare no conflicts of interest.

References

1. Rahman, M.; Sarker, S.D. *Antimicrobial Natural Products, in Annual Reports in Medicinal Chemistry*, 1st ed.; Elsevier Inc.: Amsterdam, The Netherlands, 2020; Chapter 3. [CrossRef]
2. Yi, X.; Lin, C.; Ong, E.J.L.; Wang, M.; Zhou, Z. Occurrence and distribution of trace levels of antibiotics in surface waters and soils driven by non-point source pollution and anthropogenic pressure. *Chemosphere* **2019**, *216*, 213–223. [CrossRef] [PubMed]
3. Gopal, G.; Alex, S.A.; Chandrasekaran, N.; Mukherjee, A. A review on tetracycline removal from aqueous systems by advanced treatment techniques. *RSC Adv.* **2020**, *10*, 27081–27095. [CrossRef] [PubMed]
4. Pattanayak, D.S.; Pal, D.; Mishra, J.; Thakur, C. Noble metal–free doped graphitic carbon nitride (g-C_3N_4) for efficient photodegradation of antibiotics: Progress, limitations, and future directions. *Environ. Sci. Pollut. Res.* **2022**, *30*, 25546–25558. [CrossRef] [PubMed]
5. Zedan, M.; Zedan, A.F.; Amin, R.M.; Li, X. Visible-light active metal nanoparticles@carbon nitride for enhanced removal of water organic pollutants. *J. Environ. Chem. Eng.* **2022**, *10*, 107780. [CrossRef]
6. Kumar, K.S.; Vellaichamy, B.; Paulmony, T. Visible light active metal-free photocatalysis: N-doped graphene covalently grafted with g-C_3N_4 for highly robust degradation of methyl orange. *Solid State Sci.* **2019**, *94*, 99–105. [CrossRef]
7. Li, B.; Peng, W.; Zhang, J.; Lian, J.; Huang, T.; Cheng, N.; Luo, Z.; Huang, W.; Hu, W.; Pan, A.; et al. High-Throughput One-Photon Excitation Pathway in 0D/3D Heterojunctions for Visible-Light Driven Hydrogen Evolution. *Adv. Funct. Mater.* **2021**, *31*, 2100816. [CrossRef]
8. Wang, Q.; Li, Y.; Huang, F.; Song, S.; Ai, G.; Xin, X.; Zhao, B.; Zheng, Y.; Zhang, Z. Recent Advances in g-C_3N_4-Based Materials and Their Application in Energy and Environmental Sustainability. *Molecules* **2023**, *28*, 432. [CrossRef]
9. Bai, Y.; Zheng, Y.; Wang, Z.; Hong, Q.; Liu, S.; Shen, Y.; Zhang, Y. Metal-doped carbon nitrides: Synthesis, structure and applications. *New J. Chem.* **2021**, *45*, 11876–11892. [CrossRef]
10. Bui, T.S.; Bansal, P.; Lee, B.-K.; Mahvelati-Shamsabadi, T.; Soltani, T. Facile fabrication of novel Ba-doped g-C_3N_4 photocatalyst with remarkably enhanced photocatalytic activity towards tetracycline elimination under visible-light irradiation. *Appl. Surf. Sci.* **2020**, *506*, 144184. [CrossRef]
11. Li, G.; Wang, B.; Zhang, J.; Wang, R.; Liu, H. Er-doped g-C_3N_4 for photodegradation of tetracycline and tylosin: High photocatalytic activity and low leaching toxicity. *Chem. Eng. J.* **2019**, *391*, 123500. [CrossRef]
12. Wang, M.; Guo, P.; Zhang, Y.; Lv, C.; Liu, T.; Chai, T.; Xie, Y.; Wang, Y.; Zhu, T. Synthesis of hollow lantern-like Eu(III)-doped g-C_3N_4 with enhanced visible light photocatalytic performance for organic degradation. *J. Hazard. Mater.* **2018**, *349*, 224–233. [CrossRef] [PubMed]
13. Phoon, B.L.; Ong, C.C.; Lee, K.C.; Pan, G.T.; Leo, B.F.; Chong, S.; Pan, K.L. Co-doped, tri-doped, and rare-earth-doped g-C_3N_4 for photocatalytic applications: State-of-the-art. *Catalysts* **2022**, *12*, 586. [CrossRef]
14. Chi, X.; Liu, F.; Gao, Y.; Song, J.; Guan, R.; Yuan, H. An efficient B/Na co-doped porous g-C_3N_4 nanosheets photocatalyst with enhanced photocatalytic hydrogen evolution and degradation of tetracycline under visible light. *Appl. Surf. Sci.* **2022**, *576*, 151837. [CrossRef]

15. Duan, Y.; Li, Y.; Shang, X.; Jia, D.; Li, C. Phosphorus and bismuth co-doped porous g-C_3N_4 nanosheets as an efficient visible-light-driven photocatalyst. *J. Mater. Sci. Mater. Electron.* **2020**, *31*, 1703–1714. [CrossRef]
16. Wu, K.; Chen, D.; Lu, S.; Fang, J.; Zhu, X.; Yang, F.; Pan, T.; Fang, Z. Supramolecular self-assembly synthesis of noble-metal-free (C, Ce) co-doped g-C_3N_4 with porous structure for highly efficient photocatalytic degradation of organic pollutants. *J. Hazard. Mater.* **2020**, *382*, 121027. [CrossRef]
17. Wang, M.; Guo, P.; Zhang, Y.; Liu, T.; Li, S.; Xie, Y.; Wang, Y.; Zhu, T. Eu doped g-C_3N_4 nanosheet coated on flower-like $BiVO_4$ powders with enhanced visible light photocatalytic for tetracycline degradation. *Appl. Surf. Sci.* **2018**, *453*, 11–22. [CrossRef]
18. Hu, Y.; Bi, S. Co-doping g-C_3N_4 to enhance internal electric field for robust photocatalytic degradation and H_2 production. *Chin. J. Struc. Chem.* **2022**, *41*, 2206069–2206078. [CrossRef]
19. Liu, T.; Li, Y.; Sun, H.; Zhang, M.; Xia, Z.; Yang, Q. Asymmetric structure awakened n − π* electron transition in sulfur and selenium Co-doped g-C_3N_4 with efficient photocatalytic performance. *Chin. J. Struc. Chem.* **2022**, *41*, 2206055–2206061. [CrossRef]
20. Jiang, L.; Yuan, X.; Zeng, G.; Chen, X.; Wu, Z.; Liang, J.; Zhang, J.; Wang, H.; Wang, H. Phosphorus- and sulfur-codoped g-C_3N_4: Facile preparation, mechanism insight, and application as efficient photocatalyst for tetracycline and methyl orange degradation under visible light irradiation. *ACS Sustain. Chem. Eng.* **2017**, *5*, 5831–5841. [CrossRef]
21. Xu, Y.; Liang, Y.; Yuai, Z.; Long, H.; He, Q.; Guo, K.; Zhang, Y.; Chen, D.; Xu, X.; Hu, H. Co-doping g-C_3N_4 with P and Mo for efficient photocatalytic tetracycline degradation under visible light. *Ceram. Int.* **2022**, *48*, 24677–24686. [CrossRef]
22. Starukh, H.; Praus, P. Doping of Graphitic Carbon Nitride with Non-Metal Elements and Its Applications in Photocatalysis. *Catalysts* **2020**, *10*, 1119. [CrossRef]
23. Belousov, A.S.; Suleimanov, E.V.; Fukina, D.G. Pyrochlore oxides as visible light-responsive photocatalysts. *New J. Chem.* **2021**, *45*, 22531–22558. [CrossRef]
24. Liu, Z.; Guo, W.; Liu, X.; Wu, G.; Tang, Y.; Mo, Z.; Yang, D. Study on photoelectric properties of Fe-Co codoped g-C_3N_4. *Chem. Phys. Lett.* **2021**, *781*, 138951. [CrossRef]
25. Pan, T.; Chen, D.; Fang, J.; Wu, K.; Feng, W.; Zhu, X.; Fang, Z. Facile synthesis of iron and cerium co-doped g-C_3N_4 with synergistic effect to enhance visible-light photocatalytic performance. *Mater. Res. Bull.* **2020**, *125*, 110812. [CrossRef]
26. Vignesh, S.; Nam, S.; Kim, H. Interfacial engineering of α-Fe_2O_3 coupled Co_3O_4 heterostructures anchored on g-C_3N_4 structure for enhanced electrocatalytic performance in alkaline oxygen evolution reaction. *Int. J. Hydrogen Energy* **2024**, *53*, 1445–1456. [CrossRef]
27. Dou, H.; Chen, L.; Zheng, S.; Zhang, Y.; Xu, G.Q. Band structure engineering of graphitic carbon nitride via Cu^{2+}/Cu^{+} doping for enhanced visible light photoactivity. *Mater. Chem. Phys.* **2018**, *214*, 482–488. [CrossRef]
28. Wu, Z.; Tong, Z.; Xie, Y.; Sun, H.; Gong, X.; Qin, P.; Liang, Y.; Yuan, X.; Zou, D.; Jiang, L. Efficient degradation of tetracycline by persulfate activation with Fe, Co and O co−doped g−C_3N_4: Performance, mechanism and toxicity. *Chem. Eng. J.* **2022**, *434*, 134732. [CrossRef]
29. Sun, B.-W.; Li, H.-J.; Yu, H.-Y.; Qian, D.-J.; Chen, M. In situ synthesis of polymetallic Co-doped g-C_3N_4 photocatalyst with increased defect sites and superior charge carrier properties. *Carbon* **2017**, *117*, 1–11. [CrossRef]
30. Guo, W.; Zhang, J.; Li, G.; Xu, C. Enhanced photocatalytic activity of P-type (K, Fe) co-doped g-C_3N_4 synthesized in self-generated NH_3 atmosphere. *Appl. Surf. Sci.* **2019**, *470*, 99–106. [CrossRef]
31. Ma, Y.; Sun, M.; Mominou, N.; Zuo, N.; Li, S.; Jing, C.; Wang, L. Efficient degradation of tetracycline over Co/La oriented on g-C_3N_4 with the outstanding oxygen activation property under visible light. *J. Environ. Chem. Eng.* **2022**, *10*, 107916. [CrossRef]
32. Dong, H.; Zuo, Y.; Song, N.; Hong, S.; Xiao, M.; Zhu, D.; Sun, J.; Chen, G.; Li, C. Bimetallic synergetic regulating effect on electronic structure in cobalt/vanadium co-doped carbon nitride for boosting photocatalytic performance. *Appl. Catal. B Environ.* **2021**, *287*, 119954. [CrossRef]
33. Bahadoran, A.; Najafizadeh, M.; Liu, Q.; De Lile, J.R.; Zhang, D.; Masudy-Panah, S.; Ramakrishna, S.; Fakhri, A.; Gupta, V.K. Co-doping silver and iron on graphitic carbon nitride-carrageenan nanocomposite for the photocatalytic process, rapidly colorimetric detection and antibacterial properties. *Surf. Interfaces* **2021**, *26*, 101279. [CrossRef]
34. Tasleem, S.; Tahir, M. Synergistically improved charge separation in bimetallic Co–La modified 3D g-C_3N_4 for enhanced photocatalytic H_2 production under UV–visible light. *Int. J. Hydrogen Energy* **2021**, *46*, 20995–21012. [CrossRef]
35. Xu, J.; Yu, H.; Guo, H. Synthesis and behaviors of g-C_3N_4 coupled with $LaxCo_3$-xO_4 nanocomposite for improved photocatalytic activeity and stability under visible light. *Mater. Res. Bull.* **2018**, *105*, 342–348. [CrossRef]
36. Lai, C.; Yan, H.; Wang, D.; Liu, S.; Zhou, X.; Li, X.; Zhang, M.; Li, L.; Fu, Y.; Xu, F.; et al. Facile synthesis of Mn, Ce co-doped g-C_3N_4 composite for peroxymonosulfate activation towards organic contaminant degradation. *Chemosphere* **2022**, *293*, 133472. [CrossRef]
37. Tan, L.; Tong, Y.; Yang, Y.; Ju, X.; Li, W. Degradation of tetracycline using persulfate activated by Mn, Ce co-doped g-C_3N_4 composites under visible light. *Diam. Relat. Mater.* **2023**, *140*, 110522. [CrossRef]
38. Wang, L.; Guo, X.; Chen, Y.; Ai, S.; Ding, H. Cobalt-doped g-C_3N_4 as a heterogeneous catalyst for photo-assisted activation of peroxymonosulfate for the degradation of organic contaminants. *Appl. Surf. Sci.* **2019**, *467–468*, 954–962. [CrossRef]
39. Tang, X.; Shen, W.; Li, D.; Li, B.; Wang, Y.; Song, X.; Zhu, Z.; Huo, P. Research on cobalt-doping sites in g-C_3N_4 framework and photocatalytic reduction CO_2 mechanism insights. *J. Alloys Compd.* **2023**, *954*, 170044. [CrossRef]
40. Tuna, ö.; Simsek, E.B. Synergic contribution of intercalation and electronic modification of g-C_3N_4 for an efficient visible light-driven catalyst for tetracycline degradation. *J. Environ. Chem. Eng.* **2020**, *8*, 104445. [CrossRef]

41. Zhu, Z.; Xia, H.; Wu, R.; Cao, Y.; Li, H. Fabrication of La_2O_3/g-C_3N_4 heterojunction with enhanced photocatalytic performance of tetracycline hydrochloride. *Crystals* **2021**, *11*, 1349. [CrossRef]
42. Velusamy, P.; Liu, S.; Xing, R.; Sathiya, M.; Ahmad, A.; Albaqami, M.D.; Alotabi, R.G.; Elamurugu, E.; Pandian, M.S.; Ramasamy, P. Enhanced photo-electrocatalytic performance of the nano heterostructures based on Pr^{3+} modified g-C_3N_4 and BiOI. *Int. J. Hydrogen Energy* **2022**, *47*, 32903–32920. [CrossRef]
43. Van, M.N.; Mai, O.L.T.; Do, C.P.; Thi, H.L.; Manh, C.P.; Manh, H.N.; Thi, D.P.; Danh, B.D. Fe-doped g-C_3N_4: High-performance photocatalysts in Rhodamine B decomposition. *Polymers* **2020**, *12*, 1963. [CrossRef] [PubMed]
44. Dong, S.; Lian, X.; Chen, S.; Li, H.; Liu, E.; Xu, K. Kinetic analysis and mechanism study on the photocatalytic degradation of 2,4-dinitrophenylhydrazine over surface plasmonic Ag/Cu/TiO_2 composite. *React. Kinet. Catal. Lett.* **2021**, *134*, 485–499. [CrossRef]
45. Premalatha, N.; Rajalakshmi, P.; Miranda, L.R. Photocatalytic degradation of Rhodamine B over TiO_2/g-C_3N_4 and immobilized TiO_2/g-C_3N_4 on stainless steel wire gauze under UV and visible light: A detailed kinetic analysis and mechanism of degradation. *React. Kinet. Catal. Lett.* **2022**, *135*, 1031–1046. [CrossRef]
46. Wang, H.; Zhang, J.; Wang, P.; Yin, L.; Tian, Y.; Li, J. Bifunctional copper modified graphitic carbon nitride catalysts for efficient tetracycline removal: Synergy of adsorption and photocatalytic degradation. *Chin. Chem. Lett.* **2020**, *31*, 2789–2794. [CrossRef]
47. Ren, Z.; Chen, F.; Wen, K.; Lu, J. Enhanced photocatalytic activity for tetracyclines degradation with Ag modified g-C_3N_4 composite under visible light. *J. Photochem. Photobiol. A Chem.* **2020**, *389*, 112217. [CrossRef]
48. Guo, P.; Zhao, F.; Hu, X. Boron- and europium-co-doped g-C_3N_4 nanosheets: Enhanced photocatalytic activity and reaction mechanism for tetracycline degradation. *Ceram. Int.* **2021**, *47*, 16256–16268. [CrossRef]
49. Gao, J.; Wang, Y.; Zhou, S.; Lin, W.; Kong, Y. A Facile One-Step Synthesis of Fe-Doped g-C_3N_4 Nanosheets and Their Improved Visible-Light Photocatalytic Performance. *ChemCatChem* **2017**, *9*, 1708–1715. [CrossRef]
50. Yan, W.; Yan, L.; Jing, C. Impact of Doped Metals on Urea-derived g-C_3N_4 for Photocatalytic Degradation of Antibiotics: Structure, Photoactivity and Degradation mechanisms. *Appl. Catal. B Environ.* **2019**, *244*, 475–485. [CrossRef]
51. Xu, R.; Li, J.; Sui, G.; Zhuang, Y.; Guo, D.; Luo, Z.; Liang, S.; Yao, H.; Wang, C.; Chen, S. Constructing supramolecular self-assembled porous g-C_3N_4 nanosheets containing thiophene-groups for excellent photocatalytic performance under visible light. *Appl. Surf. Sci.* **2022**, *578*, 152064. [CrossRef]
52. Jiang, J.; Cao, S.; Hu, C.; Chen, C. A comparison study of alkali metal-doped g-C_3N_4 for visible-light photocatalytic hydrogen evolution. *Chin. J. Catal.* **2017**, *38*, 1981–1989. [CrossRef]
53. Jiang, G.-J.; Wang, H.-L.; Huang, H.; Chu, S. Facile synthesis of porous Fe-doped g-C_3N_4 with highly dispersed Fe sites as robust catalysts for dinitro butyl phenol degradation by peroxymonosulfate activation. *Colloids Surfaces A Physicochem. Eng. Asp.* **2021**, *630*, 127598. [CrossRef]
54. Padervand, M.; Hajiahmadi, S. Ag/AgCl@Tubular g-C_3N_4 nanostructure as an enhanced visible light photocatalyst for the removal of organic dye compounds and biomedical waste under visible light. *J. Photochem. Photobiol. A Chem.* **2022**, *425*, 113700. [CrossRef]
55. Kang, J.-G.; Kim, Y.-I.; Cho, D.W.; Sohn, Y. Synthesis and physicochemical properties of $La(OH)_3$ and La_2O_3 nanostructures. *Mater. Sci. Semicond. Process.* **2015**, *40*, 737–743. [CrossRef]
56. Gopinath, S.; Mayakannan, M.; Vetrivel, S. Structural, optical, morphological properties of silver doped cobalt oxide nanoparticles by microwave irradiation method. *Ceram. Int.* **2022**, *48*, 6103–6115. [CrossRef]
57. Fan, J.; Qin, H.; Jiang, S. Mn-doped g-C_3N_4 composite to activate peroxymonosulfate for acetaminophen degradation: The role of superoxide anion and singlet oxygen. *Chem. Eng. J.* **2018**, *359*, 723–732. [CrossRef]
58. Ramanujam, K.; Thirupathi, T. Carbon supported g-C_3N_4 for electrochemical sensing of hydrazine. *Electrochem. Energy Technol.* **2019**, *4*, 21–31. [CrossRef]
59. Hussien, M.K.; Sabbah, A.; Qorbani, M.; Putikam, R.; Kholimatussadiah, S.; Tzou, D.M.; Elsayed, M.H.; Lu, Y.; Wang, Y.; Lee, X.; et al. Constructing B–N–P Bonds in Ultrathin Holey g-C_3N_4 for Regulating the Local Chemical Environment in Photocatalytic CO_2 Reduction to CO. *Small* **2024**, e2400724, *Online ahead of print*. [CrossRef]
60. Zhou, X.; Luo, J.; Jin, B.; Wu, Z.; Yang, S.; Zhang, S.; Tian, Y.; Fang, Y.; Hou, Y.; Zhou, X. Sustainable synthesis of low-cost nitrogen-doped-carbon coated Co_3W_3C@g-C_3N_4 composite photocatalyst for efficient hydrogen evolution. *Chem. Eng. J.* **2021**, *426*, 131208. [CrossRef]
61. Lin, H.-P.; Chen, C.-C.; Lee, W.W.; Lai, Y.-Y.; Chen, J.-Y.; Chen, Y.-Q.; Fu, J.-Y. Synthesis of a $SrFeO_{3-x}$/g-C_3N_4heterojunction with improved visible-light photocatalytic activities in chloramphenicol and crystal violet degradation. *RSC Adv.* **2016**, *6*, 2323–2336. [CrossRef]
62. Zhang, G.; Zang, S.; Lin, L.; Lan, Z.-A.; Li, G.; Wang, X. Ultrafine Cobalt Catalysts on Covalent Carbon Nitride Frameworks for Oxygenic Photosynthesis. *ACS Appl. Mater. Interfaces* **2016**, *8*, 2287–2296. [CrossRef]
63. Suyana, P.; Ganguly, P.; Nair, B.N.; Mohamed, A.P.; Warrier, K.G.K.; Hareesh, U.S. Co_3O_4–C_3N_4p–n nano-heterojunctions for the simultaneous degradation of a mixture of pollutants under solar irradiation. *Environ. Sci. Nano* **2017**, *4*, 212–221. [CrossRef]
64. Jorge, A.B.; Martin, D.J.; Dhanoa, M.T.S.; Rahman, A.S.; Makwana, N.; Tang, J.; Sella, A.; Corà, F.; Firth, S.; Darr, J.A.; et al. H_2 and O_2 Evolution from Water Half-Splitting Reactions by Graphitic Carbon Nitride Materials. *J. Phys. Chem. C* **2013**, *117*, 7178–7185. [CrossRef]

65. Yi, X.-H.; Ma, S.-Q.; Du, X.-D.; Zhao, C.; Fu, H.; Wang, P.; Wang, C.-C. The facile fabrication of 2D/3D Z-scheme g-C_3N_4/UiO-66 heterojunction with enhanced photocatalytic Cr(VI) reduction performance under white light. *Chem. Eng. J.* **2019**, *375*, 121944. [CrossRef]
66. Ahmad, N.; Kuo, C.-F.J.; Mustaqeem, M.; Sangili, A.; Huang, C.-C.; Chang, H.-T. Synthesis of novel Type-II $MnNb_2O_6$/g-C_3N_4 Mott-Schottky heterojunction photocatalyst: Excellent photocatalytic performance and degradation mechanism of fluoroquinolone-based antibiotics. *Chemosphere* **2023**, *321*, 138027. [CrossRef] [PubMed]
67. Xia, Z.; Wang, X.; Liu, K.; Wang, H.; Wang, Y.; Lu, W.; Jiang, D.; Abbasi, H.N.; Guo, Z.; Zhang, W.; et al. Preparation and photocatalytic properties of WSe_2/$BiVO_4$ p-n heterojunction photocatalytic materials. *Catal. Commun.* **2024**, *187*, 106857. [CrossRef]
68. He, D.; Yang, H.; Jin, D.; Qu, J.; Yuan, X.; Zhang, Y.-N.; Huo, M.; Peijnenburg, W.J. Rapid water purification using modified graphitic carbon nitride and visible light. *Appl. Catal. B Environ.* **2021**, *285*, 119864. [CrossRef]
69. Jing, J.; Chen, Z.; Feng, C. Dramatically enhanced photoelectrochemical properties and transformed p/n type of g-C_3N_4 caused by K and I co-doping. *Electrochim. Acta* **2019**, *297*, 488–496. [CrossRef]
70. Chang, X.; Wang, T.; Zhang, P.; Zhang, J.; Li, A.; Gong, J. Enhanced Surface Reaction Kinetics and Charge Separation of p–n Heterojunction Co_3O_4/$BiVO_4$ Photoanodes. *J. Am. Chem. Soc.* **2015**, *137*, 8356–8359. [CrossRef]
71. Liu, Y.; Gong, Y.; Cui, X.; Yu, H.; Qin, W.; Cui, X.; Huo, M. Synthesis of O-doped C_3N_4 decorated with C_3N_4 quantum dots: Construction of a homo junction photocatalyst for the enhanced photocatalytic degradation of tetracycline. *J. Taiwan Inst. Chem. Eng.* **2022**, *138*, 104457. [CrossRef]
72. Zheng, H.; Ji, Y.; Li, S.; Li, W.; Ma, J.; Niu, J. Ecotoxicity and resistance genes induction changing of antibiotic tetracycline degradation products dominated by differential free radicals. *Environ. Res.* **2023**, *227*, 115427. [CrossRef]
73. Guo, L.; Zhao, L.; Tang, Y.; Zhou, J.; Shi, B. Peroxydisulfate activation using Fe, Co co-doped biochar and synergistic effects on tetracycline degradation. *Chem. Eng. J.* **2023**, *452*, 139381. [CrossRef]
74. Zheng, S.; Ding, B.; Qian, X.; Yang, Y.; Mao, L.; Zheng, S.; Zhang, J. High efficiency degradation of tetracycline and rhodamine B using Z-type $BaTiO_3$/γ-Bi_2O_3 heterojunction. *Sep. Purif. Technol.* **2022**, *278*, 119666. [CrossRef]
75. Wang, W.; Li, Z.; Wang, H.; Luo, H.; Meng, Z.; Liu, X.; Liu, L.; Chen, W.; Jin, B.; Huang, K.; et al. Construction of novel dual Z-scheme g-C_3N_4/$ZnFe_2O_4$/Ag_2CO_3 heterojunction with enhanced visible-light-driven performance for tetracycline degradation and bacterial inactivation. *J. Environ. Chem. Eng.* **2023**, *11*, 111421. [CrossRef]
76. Chen, Z.; Fu, M.; Yuan, C.; Hu, X.; Bai, J.; Pan, R.; Lu, P.; Tang, M. Study on the degradation of tetracycline in wastewater by micro-nano bubbles activated hydrogen peroxide. *Environ. Technol.* **2022**, *43*, 3580–3590. [CrossRef] [PubMed]
77. Zhou, J.; Pan, F.; Wang, T.; Zhang, Y.; Yao, Q.; Zhu, C.; Zhu, Y.; Ma, H.; Niu, J. Controlled synthesis of water–soluble Pt nanoclusters and their co–catalysis with RuO_2–IrO_2 for electrochemical degradation of tetracycline. *Sep. Purif. Technol.* **2022**, *295*, 121323. [CrossRef]
78. Wang, Y.; Ding, L.; Liu, C.; Lu, Y.; Wu, Q.; Wang, C.; Hu, Q. 0D/2D/2D $ZnFe_2O_4$/$Bi_2O_2CO_3$/BiOBr double Z-scheme heterojunctions for the removal of tetracycline antibiotics by permonosulfate activation: Photocatalytic and non-photocatalytic mechanisms, radical and non-radical pathways. *Sep. Purif. Technol.* **2022**, *283*, 120164. [CrossRef]
79. Moradi, S.; Isari, A.A.; Hayati, F.; Kalantary, R.R.; Kakavandi, B. Co-implanting of TiO_2 and liquid-phase-delaminated g-C_3N_4 on multi-functional graphene nanobridges for enhancing photocatalytic degradation of acetaminophen. *Chem. Eng. J.* **2021**, *414*, 128618. [CrossRef]
80. Akhter, P.; Nawaz, S.; Shafiq, I.; Nazir, A.; Shafique, S.; Jamil, F.; Park, Y.-K.; Hussain, M. Efficient visible light assisted photocatalysis using ZnO/TiO_2 nanocomposites. *Mol. Catal.* **2023**, *535*, 112896. [CrossRef]
81. Wang, X.; Lu, M.; Ma, J.; Ning, P.; Che, L. Synthesis of K-doped g-C_3N_4/carbon microsphere@graphene composite with high surface area for enhanced adsorption and visible photocatalytic degradation of tetracycline. *J. Taiwan Inst. Chem. Eng.* **2018**, *91*, 609–622. [CrossRef]
82. Hu, J.; Zhao, G.-Q.; Wu, L.-X.; Sun, C.; Long, X.; Long, X.-Q.; Jiao, F.-P. Designing and Fabricating a Vulcanized ZnAl LDH-Modified g-C_3N_4 Heterojunction for Enhanced Visible-Light-Driven Photocatalytic Degradation Activity. *Ind. Eng. Chem. Res.* **2022**, *61*, 15225–15239. [CrossRef]
83. Rezaei, S.S.; Kakavandi, B.; Noorisepehr, M.; Isari, A.A.; Zabih, S.; Bashardoust, P. Photocatalytic oxidation of tetracycline by magnetic carbon-supported TiO_2 nanoparticles catalyzed peroxydisulfate: Performance, synergy and reaction mechanism studies. *Sep. Purif. Technol.* **2021**, *258*, 117936. [CrossRef]
84. Tang, J.; Wang, J.; Tang, L.; Feng, C.; Zhu, X.; Yi, Y.; Feng, H.; Yu, J.; Ren, X. Preparation of floating porous g-C_3N_4 photocatalyst via a facile one-pot method for efficient photocatalytic elimination of tetracycline under visible light irradiation. *Chem. Eng. J.* **2022**, *430*, 132669. [CrossRef]
85. Hunge, Y.M.; Yadav, A.A.; Kang, S.-W.; Kim, H. Photocatalytic degradation of tetracycline antibiotics using hydrothermally synthesized two-dimensional molybdenum disulfide/titanium dioxide composites. *J. Colloid Interface Sci.* **2022**, *606*, 454–463. [CrossRef] [PubMed]
86. Divakaran, K.; Baishnisha, A.; Balakumar, V.; Perumal, K.N.; Meenakshi, C.; Kannan, R.S. Photocatalytic degradation of tetracycline under visible light using TiO_2@sulfur doped carbon nitride nanocomposite synthesized via in-situ method. *J. Environ. Chem. Eng.* **2021**, *9*, 105560. [CrossRef]

87. Feng, Y.; Chen, G.; Zhang, Y.; Li, D.; Ling, C.; Wang, Q.; Liu, G. Superhigh co-adsorption of tetracycline and copper by the ultrathin g-C_3N_4 modified graphene oxide hydrogels. *J. Hazard. Mater.* **2022**, *424*, 127362. [CrossRef] [PubMed]
88. Kandi, D.; Behera, A.; Sahoo, S.; Parida, K. CdS QDs modified BiOI/Bi_2MoO_6 nanocomposite for degradation of quinolone and tetracycline types of antibiotics towards environmental remediation. *Sep. Purif. Technol.* **2020**, *253*, 117523. [CrossRef]
89. Preeyanghaa, M.; Erakulan, E.; Thapa, R.; Ashokkumar, M.; Neppolian, B. Scrutinizing the role of tunable carbon vacancies in g-C_3N_4 nanosheets for efficient sonophotocatalytic degradation of Tetracycline in diverse water matrices: Experimental study and theoretical calculation. *Chem. Eng. J.* **2023**, *452*, 139437. [CrossRef]
90. Wang, Y.; Gao, Q.; You, Q.; Liao, G.; Xia, H.; Wang, D. Porous polyimide framework: A novel versatile adsorbent for highly efficient removals of azo dye and antibiotic. *React. Funct. Polym.* **2016**, *103*, 9–16. [CrossRef]